Volume 32 | Number 2 | February 2017 | Pages 203–422

JAAS

Journal of Analytical Atomic Spectrometry

rsc.li/jaas

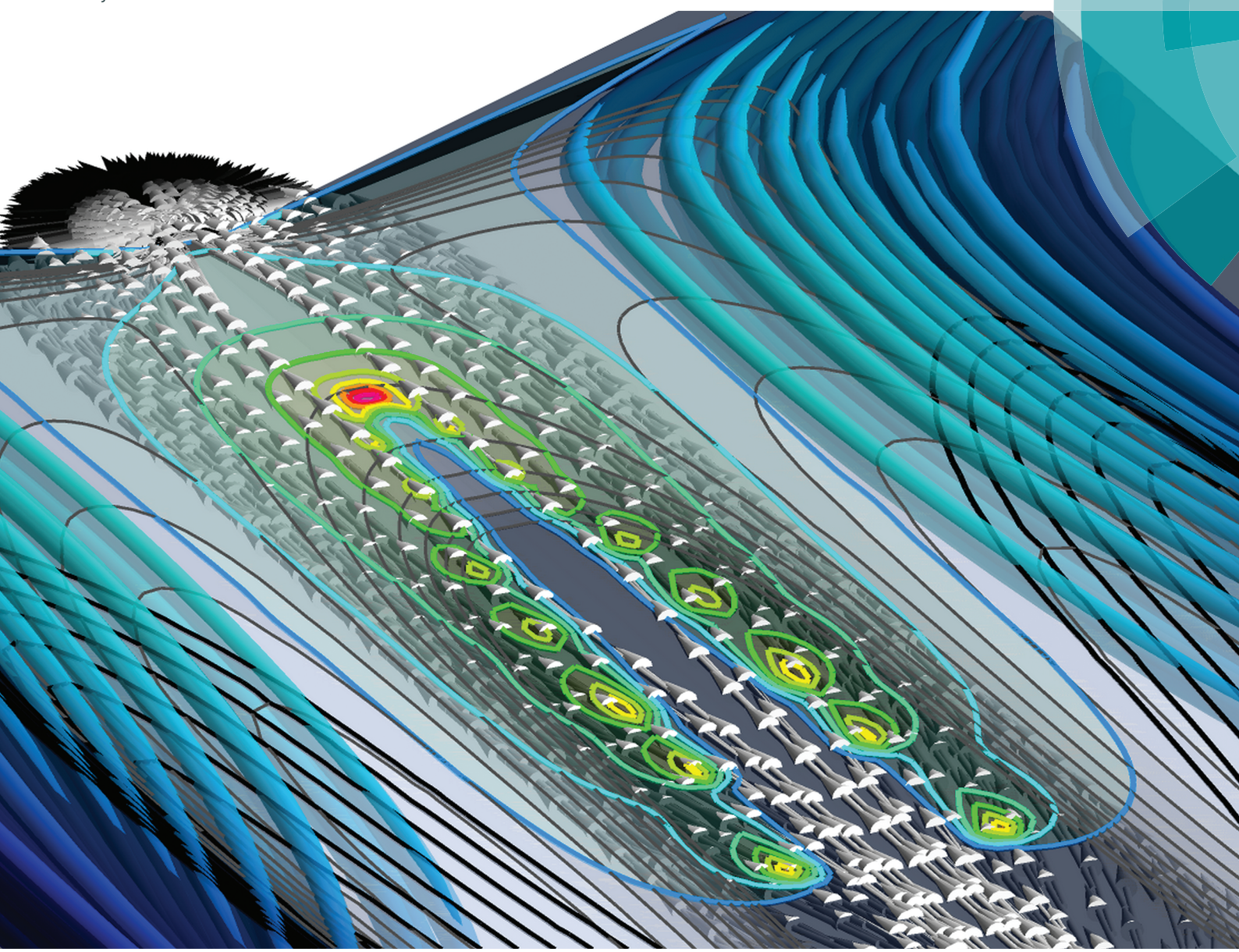

ISSN 0267-9477

ROYAL SOCIETY OF CHEMISTRY

TUTORIAL REVIEW

Annemie Bogaerts and Maryam Aghaei

Inductively coupled plasma-mass spectrometry: insights through computer modeling

JAAS

TUTORIAL REVIEW

Cite this: *J. Anal. At. Spectrom.*, 2017, **32**, 233

Inductively coupled plasma-mass spectrometry: insights through computer modeling

Annemie Bogaerts and Maryam Aghaei

Received 9th November 2016
Accepted 7th December 2016

DOI: 10.1039/c6ja00408c

www.rsc.org/jaas

In this tutorial review paper, we illustrate how computer modeling can contribute to a better insight in inductively coupled plasma-mass spectrometry (ICP-MS). We start with a brief overview on previous efforts, studying the fundamentals of the ICP and ICP-MS, with main focus on previous modeling activities. Subsequently, we explain in detail the model that we developed in previous years, and we show typical calculation results, illustrating the plasma characteristics, gas flow patterns and the sample transport, evaporation and ionization. We also present the effect of various experimental parameters, such as operating conditions, geometrical aspects and sample characteristics, to illustrate how modeling can help to elucidate the optimal conditions for improved analytical performance.

1. Introduction

The inductively coupled plasma (ICP) is one of the most popular ion sources for mass spectrometry.[1,2] It is routinely used for the elemental analysis of various types of samples, in liquid, gaseous or solid state, the latter in combination with special sample introduction methods, such as laser ablation (LA). When the sample to be analysed is introduced into the plasma (as aerosol, liquid or solid particles), it will be subject to desolvation, evaporation, ionization and excitation. The ions created in this way can be measured with a mass spectrometer, giving rise to ICP-MS. Alternatively, the characteristic photons emitted by the excited species can be detected by optical emission spectrometry, yielding ICP-OES.

Since the demonstration of the analytical capabilities of ICP-MS in 1980,[3] this technique has gained general acceptance in all types of laboratories, ranging from academic research to service labs and industry. However, to continue improving the analytical applications, fundamental studies of the ICP are indispensable. Many research groups have studied the basic characteristics of the ICP, either by experiments[4–62] or computer modeling,[63–133] although the latter were not always applied to ICPs used for analytical spectrochemistry applications. In the next section, we will give a brief overview of some experimental studies published in literature and relevant for the modeling

Research Group PLASMANT, Dept. of Chemistry, University of Antwerp, Belgium. E-mail: annemie.bogaerts@uantwerpen.be; Maryam.aghaei@uantwerpen.be

Annemie Bogaerts is full professor of physical chemistry at the University of Antwerp since 2012, and head of the interdisciplinary research group PLASMANT (Plasma, Laser Ablation and Surface Modeling ANTwerp). During her own PhD (1996) and postdoc research, she modeled glow discharges and laser ablation for analytical spectrometry applications. Later on, she extended her research to other applications of plasmas, and founded the group PLASMANT. The group counts over 30 researchers, and focuses on modeling and experiments for plasma and plasma–surface interactions, for environmental, energy, medical and materials science applications, besides analytical chemistry.

Maryam Aghaei is a post-doc researcher at the PLASMANT group, University of Antwerp. She is interested in modeling physical phenomena and specifically gas dynamics of plasmas. As a result, a model for nanosecond pulsed laser ablation was developed during her master study (Photonics, Laser and Plasma Research Institute, Tehran). Subsequently, she developed a computational model for an inductively coupled plasma (ICP) torch coupled to a mass spectrometer during her doctorate study (Physics, Antwerp, 2014). Her current work is to optimize the transport efficiency of injected material trough the ICP torch, funded by a research grant from the Research Foundation Flanders (FWO).

work presented here, and (especially) of computational investigations reported earlier. It is not our intention to provide a complete literature overview on the experimental work, which is beyond the scope of this tutorial review paper on modeling, but only to mention some key publications relevant for this paper, from the various groups working in this field. After this literature overview, we will explain in more detail the model developed within our group PLASMANT and show typical calculation results for a wide range of operating conditions, geometrical aspects and sample parameters.

2. Previous fundamental studies in the literature – a brief overview

2.1. Experimental investigations

In ICP-MS, the ions are sampled from a sampling cone inserted into the plasma. This (metal) sampling cone is relatively cool compared to the plasma temperature, so it causes changes in the composition of the plasma gases that are in contact with the metal surface. Indeed, a boundary layer of cooler gases is formed near the surface of the metal. A detailed discussion of this boundary layer between the plasma and the sampler orifice, as well as of sample introduction, ionization and ion extraction in ICP-MS, was already presented back in 1981 by Houk *et al.*[4] Subsequently, several studies have been reported on the ICP characteristics in the presence of a MS sampling interface. For instance, the groups of Farnsworth, Hieftje and Houk studied the downstream region from the sampling interface,[5–8] but they did not give information on changes in the plasma itself. Several groups also investigated the plasma region itself,[9–17] but without comparison of plasma characteristics in the presence of the interface to the same characteristics in the absence of the interface. On the other hand, a detailed comparison of the plasma characteristics with and without sampling interface was performed by the groups of Houk,[18,19] Farnsworth[20] and Hieftje.[21] Ma *et al.*[20] used laser induced fluorescence (LIF) to investigate the effect of the sampling interface on the analyte atom and ion distributions in the ICP, while Lehn *et al.*[21] reported that the presence of the sampling interface causes changes in the fundamental plasma characteristics, such as electron number density and gas temperature.

A large number of investigations were also carried out to study the effect of the ICP operating conditions on the plasma characteristics, to optimize the analytical performance.[22–32] However, most of these studies focused on the overall instrument performance and not on the plasma itself.[24–29] Macedone *et al.*[22] studied the effects of the rf power, nebulizer flow rate, sample composition and torch-shield configuration on the ion transport efficiency through the ICP-MS interface by LIF, both upstream and downstream from the sampler. In a later paper, the same group also showed that the barium ion number density in the plasma upstream from the sampler drops upon reducing the sampling depth.[32] Gamez *et al.* performed Thomson and Rayleigh scattering measurements, and reported that the perturbation in the radial distribution of the electron density, as well as the drop in gas temperature due to the MS interface, varies with applied rf power, central gas flow rate and sampling depth.[30,31]

Next to the ICP operating conditions, the effect of the geometrical parameters has also been of considerable interest. In 1983, Gray and Date[33] already reported that for sampling the bulk plasma, larger sampler orifice diameters (at least 0.2 mm in diameter) were required, compared to those in boundary layer sampling (*i.e.*, 50–80 μm diameter range). However, these larger orifice diameters resulted in another problem, *i.e.*, the development of a secondary discharge between the plasma and the sampling cone, as explained also by Houk and coworkers[4,19] and by Hieftje *et al.*[34] On the other hand, Lichte *et al.*[35] reported that the sampling orifice might become smaller due to deposition of material, and the metal to metal oxide ratios change as the deposit grows. Crain *et al.*[36] reported that the ratio of sampler and skimmer orifice diameters also affects the matrix effects. Vaughan and Horlick[37] varied the sampler and skimmer orifice diameters, showing that the sampler orifice diameter has a major impact on the signal characteristics, more specifically for the MO^+/M^+ signal ratio in the case of oxide forming elements. The same was also reported by Longerich *et al.*[38] In addition, it was reported that the sampling orifice changes the response of the signal to changes in the nebulizer flow rate.[37,38] Günther *et al.* also reported that many background intensities can be reduced by up to two orders of magnitude, upon decreasing the sampler cone orifice size (from 0.7 to 0.5 mm), while maintaining comparable sensitivity.[39] Finally, Taylor and Farnsworth recently studied the effect of skimmer cone design (for five commercially available skimmer designs) on the shock formation and ion transmission efficiency in the vacuum interface of an ICP-MS,[40] and reported, among others, that the transmission efficiency increased upon increasing skimmer orifice diameter. These observations all suggest that the use of interfaces with different orifice sizes can affect the detection efficiency.

In addition to the effect of sampler and skimmer orifice diameter, the position of the sampler also has been the subject of experimental studies. Gamez *et al.* investigated the effect of sampling position on the plasma characteristics of an ICP, and observed a drop in plasma temperature upon shorter distance between MS interface and ICP load coil.[31] Likewise, Macedone *et al.* reported a drop in the barium ion number density in the plasma upstream from the sampler upon decreasing the sampling position.[32]

In order to optimize the efficiency of material transport, studying recirculation of the gas and optimizing the flow patterns is also of crucial importance. Although the operating and geometrical parameters can also influence the flow path lines inside the torch, this behavior has not yet been thoroughly investigated experimentally, because of the difficulties in measuring the gas flow characteristics along the entire ICP torch, and because researchers are mostly interested in the region of the coil and after the coil (in the case of ICP-OES) and in the sampler cone region (in the case of ICP-MS). Nevertheless, Houk and coworkers have confirmed the presence of recirculation by high-speed photography of plasma fluctuations.[41]

Several dedicated studies have also been performed on the material transport in the ICP. Olesik investigated the fate of individual sample droplets, by means of a monodisperse dried microparticulate injector (MDMI), looking at the diffusion process of a single element (Sr) after injection of droplets, or particles from dried droplets, by means of laser induced fluorescence[42] and side-on optical emission spectroscopy.[43] Kinzer and Olesik[44,45] as well as Lazar and Farnsworth[46,47] reported a drop in the number of analyte ions produced from each droplet of the sample solution upon addition of high concentrations of concomitant species. Furthermore, Olesik and coworkers studied the correlations between the number of scattering events from an individual incompletely desolvated droplet on the one hand, and the increase in atom emission intensity and decrease in ion emission intensities on the other hand.[48] Monnig and Koirtyohann[49] showed that the completion of the aerosol droplet vaporization can explain the transition from the initial radiation zone to the analytical zone of the ICP.

The trajectory and diffusion of analytes throughout the ICP was also investigated by Houk and coworkers.[50–53] The authors made a comparison between wet droplets and solid particles by measuring the emission from vapor clouds surrounding the aerosol droplets or particles.[51,52] A comparison between the dried solution aerosols from a microconcentric nebulizer and solid particles from LA was also performed by the groups of Houk, Montaser and Niemax.[53–55] Montaser and coworkers determined the droplet velocities in the ICP by means of particle image and particle tracking velocimetry.[54] Niemax and coworkers investigated the effect of injector gas flow rate, droplet diameter and amount of analyte on the spatial positions of analyte atomization and ionization, by means of end-on and side-on OES and applying monodisperse microdroplets (MDMDs).[55–58]

Finally, Günther and colleagues applied 2D OES and ICP-quadrupole (Q)MS of individual particles, to study the evaporation process of laser-produced aerosols and the subsequent diffusion losses inside the ICP,[59,60] and they reported that larger particles may vaporize incompletely or at different axial positions inside the ICP because of composition-dependent melting and vaporization enthalpies.[61] In a recent study, Borovinskaya *et al.* applied side-on optical imaging of Sr from single droplets, to understand the temporal separation of ion signals in ICP-MS.[62]

2.2. Computational investigations

Besides experimental studies, computer modeling can also be very useful to obtain a better understanding of the plasma characteristics, gas flow dynamics and material transport in the ICP. Various modeling efforts have been reported in literature by several groups,[63–133] although it should be mentioned that not all of these studies were dedicated to an analytical ICP.

Perhaps the first model for a spectrochemical ICP was proposed by Barnes, based on a 2D energy equation with 1D electromagnetic field equations, to calculate the 2D temperature and velocity profiles in the torch, as well as the plasma and analyte emission profiles.[63] This model did, however, not yet account for the local cooling of the plasma due to the presence of particles or aerosols.

Most of the pioneering work on ICP modeling was performed by Mostaghimi, Proulx and Boulos.[64–82] By means of a so-called "particle-source-in-cell" (PSI-cell) method, this group was able to describe the injection of powders into an ICP torch, assuming 1D electro-magnetic fields.[64–67] They reported that the plasma–particle interaction can have a significant effect on the temperature in the plasma. The authors also compared two different algorithms for calculating the gas flow and temperature in an ICP, indicating that the mathematical model formulation and the numerical solution method can substantially affect the stability and convergence of the solution.[68] In these studies, the ICP torch was not connected to a MS interface, so the relevance for ICP-MS is somewhat limited. Moreover, the gas viscosity was ignored in their model, and the operating conditions were not always applicable for analytical chemistry purposes.

The same group, however, also developed a model for calculating the 2D emission pattern from a spectrochemical ICP, in collaboration with Barnes.[69] The authors calculated the gas flow and temperature, as well as the population density of different species in the plasma, assuming local thermodynamic equilibrium (LTE), and they estimated the emission pattern for different atomic and ionic lines. Subsequently, they proposed a two-temperature model for calculating the 2D gas flow and temperature profiles in an rf ICP torch, and they reported that deviations from LTE were relatively small at atmospheric pressure, but substantial deviations from LTE were noted at reduced pressure, resulting in lower radiation losses and higher wall conduction.[70] In a follow-up study, they investigated the effect of the induction frequency in the range of 3–40 MHz, for an argon plasma at atmospheric pressure, and found that higher frequencies yielded a larger difference between the electron and the atom/ion temperatures.[71]

Furthermore, the same group also investigated turbulence in the ICP, by means of a so-called standard k–ε model, showing the presence of both laminar and turbulent regimes in the same flow field.[72] They also presented a more realistic 2D representation of the electromagnetic fields in the ICP,[73,74] as well as a 3D laminar model for predicting the mixing pattern of single and multiple cold jets with a transverse plasma flow.[75]

To analyse the chemical reactions in an ICP chemical reactor, the same group also developed a chemical equilibrium model and a kinetic model, and they compared the gas flow and the temperature and concentration profiles calculated with both models.[76,77] Furthermore, they studied the influence of radiative energy losses on the flow and temperature profiles, both for a pure argon ICP and an argon plasma with small concentrations of copper vapor.[78] Besides argon plasmas, the group also performed computer simulations for helium ICPs[79,80] and argon–nitrogen mixtures.[81] Finally, they proposed an extended geometry for the electromagnetic fields, hence not limited to the torch diameter,[82] which allows the use of simpler boundary conditions in the so-called 'open torch' modeling, compared to 'closed' torches, *i.e.*, not taking into account the gas flow to the ambient environment.[83]

Other modeling activities were reported by Benson, Montaser and colleagues, to computationally investigate droplet heating, desolvation and evaporation in an ICP.[84–86] A two-phase continuum flow computer model was developed to calculate the total desolvation rate of sample droplets. This model was extended by equations for the trajectories of the particles throughout the plasma, in order to describe the behavior of aerosol droplets from a direct injection high efficiency nebulizer (DIHEN). The authors compared two separate techniques, *i.e.*, based on the Stokes equation and a direct simulation Monte Carlo treatment, for determining the droplet trajectories.[84,85] Furthermore, they also studied droplet coalescence along with transport, heating and desolvation, predicting spatial maps of the droplet number and mass densities within the ICP for a conventional nebulizer-spray chamber arrangement, a DIHEN, and a large bore DIHEN (LB-DIHEN).[86]

Likewise, Horner and Hieftje also studied particle melting, boiling and vaporization inside the ICP torch, assuming that the particles could travel along the ICP symmetry axis without significant scatter.[87] However, like in the particle transport models of Benson *et al.*, a separate code was required to produce the initial set of plasma conditions. Hence, this model did not yet account for the energy loss by the plasma due to droplet evaporation. Shan and Mostaghimi developed a model to study the plasma behavior within the ICP as well as the droplet desolvation and trajectories, by means of a stochastic technique combined with a Monte Carlo approach.[88] However, ionization and the presence of the MS interface were not included in this model.

Colombo and coworkers also did a lot of modeling work for ICP torches, albeit mostly for higher power values (*e.g.*, 5–25 kW) than typically used for analytical chemistry.[89–105] For instance, they developed a 3D model by means of the commercial computational fluid dynamics code FLUENT, taking into account the helicoidal coil and showing the effects of its non-axisymmetry on the plasma behavior.[92] Furthermore, they studied different coil configurations, such as planar, elliptical, and double-stage.[93,94] As mentioned above, this model was typically applied for higher power (*e.g.*, 25 kW),[95] but in collaboration with Mostaghimi, they also studied the behavior at a lower power of 300 W and a frequency of 40 MHz, chosen for spectroscopic analysis.[96]

The same group also investigated the trajectory and heating of powders injected into the ICP with an injector gas, accounting for the coupling between particles and plasma, but again in a higher power range (10–25 kW).[97,98] The effects of powder feed rate, injection probe position and frequency on the plasma and particle temperature were investigated.[99] The authors also presented a turbulent model for an ICP torch operating at a power range of 10–15 kW.[100,101] Furthermore, they studied two-temperature thermodynamic and transport properties of argon–hydrogen and nitrogen–hydrogen[102] as well as carbon–oxygen[103] plasmas. Finally, they also presented a model for the optimization of the reaction chamber for silicon nanoparticle synthesis by an rf ICP.[104,105]

Shigeta and coworkers also did outstanding computational work on rf ICP torches.[106–116] The aim of most of their studies was the production of nanoparticles.[106–108] The size of the torches under study (*i.e.*, a length of 180 mm and a diameter of 45 mm) was larger than the typical torches used in analytical spectrochemistry, while the external power (5–16 kW) was higher and the current frequency (4 MHz) was lower than the ones used in ICP-MS/OES. Both 1D and 2D models were applied to study the effects of the gas flow profiles on the synthesized nanoparticles.[109,110] Later, a time-dependent 3D numerical simulation was conducted to investigate the thermo-fluid dynamics of an argon rf ICP with a direct-current (dc) plasma jet assistance, considering non-uniform density and temperature profiles in time and space, as well as turbulence generation and suppression.[111] The flow field had a complicated 3D structure with a recirculating zone due to Lorentz forces. As a result, the injected cold gas tended to avoid the high-temperature plasma region. The largest vortex structure, at approximately 10 000 K, remained in the plasma region, whereas small cold eddies were generated near the top wall of the torch and transported downstream, avoiding the plasma region.[112] The same authors also studied the effect of the quenching gas flow rate and the powder feed rate on the number density, diameter and specific surface of the produced metal nanoparticles,[113] as well as the effects of several cooling methods on the formation mechanisms of the nanoparticles in distinctive thermo-fluid fields.[114] Finally, non-equilibrium modeling of argon–oxygen and argon–hydrogen ICPs was performed without thermal and chemical equilibrium assumptions.[115,116]

Benoy also developed a model for an ICP, based on non-LTE, by solving the conservation laws of mass, momentum and energy.[117] The model accounted for the macroscopic fluid dynamics, as well as the atomic collisional and radiative processes and was applied to a relatively large ICP at low frequency (3 MHz), as well as to a relatively small ICP at high frequency (100 MHz). While the description of the first ICP was found to be relatively simple, the second ICP turned out to be much more complicated to simulate. Indeed, due to the high energy densities, steep gradients and strong transport, the exact knowledge of the transport processes was found to be crucial, and the numerical solution was less stable. Finally, Degrez and coworkers also developed some models for an ICP, but this was for the purpose of space vehicle re-entry experiments in a wind tunnel, using a so-called plasmatron ICP operating up to 1.2 MW, hence not for analytical spectrochemistry conditions.[118–121]

To our knowledge, the first theoretical studies directly relevant for ICP-MS were conducted by Douglas and French, who developed an approximate model of ideal gas flow through the sampling cone of an ICP, *i.e.*, the so called "hemispherical-sink model", assuming that the gas flow toward the nozzle behaves like a flow in a duct.[122] To a first approximation, the area of the duct at a specific point with radial distance R in a spherical geometry was taken equal to the area of the sampler orifice plus $2\pi R^2$. This allowed the authors to obtain the Mach number as a function of R and subsequently, they could achieve information on typical fluid quantities, such as temperature and number density. Spencer *et al.* applied a Direct Simulation Monte Carlo algorithm to model the flow of neutral argon gas through the first vacuum stage of the ICP-MS, and therefore,

they were the first to describe the effect of the sampler cone in ICP-MS.[123,124] Their calculation results were in good agreement with those of the approximate hemispherical sink model of Douglas and French. They were able to obtain plasma velocity data in the region a few millimeters upstream from the sampler, in reasonable agreement with experiments. Furthermore, they provided a formula for the Mach number as a function of distance along the central axis, which may be useful to predict the variation of velocity, density and temperature along the central axis near the sampler.[124] However, they did not incorporate a plasma description in their models, and thus the upstream density and plasma temperature gradients were not calculated.

We believe that the first "self-consistent" model for an atmospheric pressure ICP, operating at typical analytical chemistry conditions, and focusing on the gas flow dynamics and plasma formation, was presented by Lindner and Bogaerts.[125] To our knowledge, this is indeed the first model for typical analytical spectrochemistry conditions, which takes viscosity and ionization into account, and which can trace the gas flow and calculate the plasma characteristics inside the entire ICP. For this purpose, a dedicated kinetic model was developed in which the transport parameters were calculated for arbitrary mixtures of atomic species, based on the data from the pure elements, and the calculated values for viscosity and thermal conductivity were found in good agreement with literature data in the relevant temperature range. Therefore, the applicability of this model is not limited to specific mixtures for which the data (*i.e.*, species and relative concentrations) are known, but the model can be applied to a wider variety of gas mixtures, including carrier gas and sample material. Especially the ionization degree is dependent on the actual composition of the plasma, which strongly affects the transport parameters. A validation of this model by experiments was also provided,[126] as will be illustrated in Section 3.4 below.

The latter model served as the basis for the further modeling work performed within our group PLASMANT.[127–133] Indeed, in a follow-up study, we described the ICP torch connected to a MS sampler cone, considering the large pressure drop from upstream to downstream (*i.e.* 1 atm to 1 Torr).[127] We believe that this model showed for the first time how the plasma characteristics are affected by a cool, grounded sampler, and by the sudden pressure drop behind it. We investigated the plasma behavior in a wide range of gas flow rates and applied power,[128] and by varying the position and diameter of the sampling cone.[129] Furthermore, we also studied the recirculation of the gas flow, in order to optimize the flow behavior inside the ICP torch.[130] All this work formed the subject of the PhD thesis of Aghaei.[131] Recently, we extended the model, to incorporate the behavior of analyte material. In first instance, we focused on elemental particles, as relevant for LA-ICP-MS.[132,133] The inserted particles were followed throughout the ICP, up to the evaporation step.[132] Finally, we also included ionization of the elemental particles, taking Cu as a case study.[133] This model allows us to trace the particles, and to determine their position, their phase (liquid, vapor or ionized), velocity and temperature, both in the ICP torch and at the sampler orifice. Thus, we can determine the shape and position of the ion clouds, originating from either the Ar flow or the inserted sample material, which is of interest for both OES and MS studies.

In the next section, we will give more details on the characteristic features of the model, including the assumptions made, the equations to be solved and the input data and boundary conditions of the model. Also the validation of the model with experiments will be illustrated. Subsequently, typical calculation results will be presented, to indicate what type of information can be obtained from the model, and how modeling can contribute to a better insight in the underlying mechanisms and help to improve the applications.

3. Description of the modeling work

3.1. Modeling geometry, assumptions and input conditions

The model that we developed over the previous years is made within the commercial computational fluid dynamics program FLUENT (ANSYS),[134] but we added several self-written modules as user defined functions (UDFs), as will be explained below. We assume a two-dimensional (2D) axisymmetric geometry, as presented in Fig. 1. We performed calculations for various diameters of the injector gas inlet and sampler orifice, as well as for various distances between the sampler and the load coil (see Table 1).

The gas enters through the three concentric tubes of the ICP torch, *i.e.*, the injector gas inlet, auxiliary inlet and outer inlet, and flows into an open ambient gas, which is for simplicity assumed to be argon in our model. The gas flow rate through the outer inlet, the auxiliary inlet and the injector gas inlet was varied in a certain range, as indicated in Table 1. The flow rate of the ambient gas is determined by the pressure difference between the ambient pressure (101 325 Pa) and the pressure set for the exhaust (101 225 Pa). The flow is assumed to be laminar, which is justified because the Reynolds number is typically in the order of 100 for regions close to the sampler, and certainly below 1000 for regions close to the inlets, for the conditions under study, so it is far from the turbulence regime.

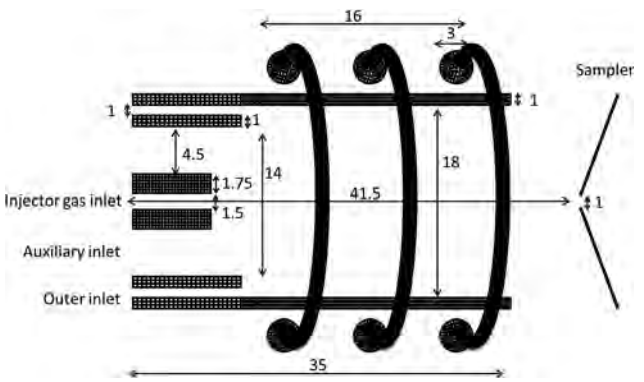

Fig. 1 Schematic picture of the ICP geometry assumed in the 2D axisymmetric model. The dimensions are given in mm. Note that the distance between sampler and load coil, as well as the diameter of the sampler and injector gas inlet were varied in our simulations (see the range in Table 1).

Table 1 Operating conditions, sample characteristics and geometrical parameters for which the model is applied

Operating conditions	
Frequency	27 MHz
Input power	750–1500 W
Injector gas flow rate	Ar; 0.3–2.5 L min^{-1}
Auxiliary gas flow rate	Ar; 0.3–1.2 L min^{-1}
Coolant gas flow rate	Ar; 12–16 L min^{-1}
Ambient pressure	101 325 Pa
Exhaust pressure	101 225 Pa
Pressure downstream the sampler cone	1.32×10^{-3} atm (1 Torr)
Inlet gas temperature	297 K
Sampler cone temperature	500 K
Sample characteristics (Cu)	
Particle diameter	10 nm – 100 nm – 1 μm – 10 μm – 100 μm
Mass loading flow rate	1 ng s^{-1} to 500 μg s^{-1}
Injection position	Entire injector gas inlet; on-axis; off-axis
Geometrical parameters	
Injector inlet diameter	1.5–2 mm
Sampler orifice diameter	1–2 mm
Sampler distance from the load coil	7–17 mm

Note that the calculation region extends further than only the inside of the torch, to enable a proper description of the gas flow dynamics, and to allow simpler boundary conditions for the model. For instance, this approach allows us to set the electric field equal to zero at the boundary, without affecting the plasma behavior, which can be considered equivalent to the metal shielding box around the ICP, preventing the rf radiation from entering the laboratory. The entire calculation region has an axial length of 45 mm (or even 150 mm when no sampling cone is present, see Section 4.3 below) and a radius of 100 mm. The geometry is subdivided into *ca.* 15 000 cells (in the presence of a sampler) or 23 000 cells (without sampler), of which the largest fraction is located inside the torch and in the region directly behind the torch.

In our geometry, the coils are assumed to be perpendicular to the ICP torch (see Fig. 1), which allows to use a 2D axisymmetric model. However, in real ICP instruments, the coils wrap the torch not exactly perpendicular, so the plasma will not be fully symmetric, and modeling in 3D should provide a higher accuracy. However, Colombo *et al.* reported that the asymmetric effect of the coil orientation on the plasma temperature drops upon increasing the frequency of the external current from 3 MHz to 13.56 MHz.[99] As we consider a frequency of 27 MHz in all our calculations, we expect that the temperature profile should be rather close to symmetric.

The model assumes local thermodynamic equilibrium (LTE), and a motivation for this was given by Lindner and Bogaerts.[125] Although this is an approximation, the use of a two-temperature model does not necessarily yield different temperatures for electrons and heavy species.[83] Moreover, Mostaghimi *et al.* reported that for an argon ICP at atmospheric pressure, deviations from LTE are relatively small,[70] so we believe that the LTE assumption closely approaches the accuracy of non-LTE models at the conditions under study. Furthermore, using the LTE assumption has the advantage that the model can be more easily formulated in a self-consistent way and it requires less other assumptions, *e.g.*, on power coupling and energy transfer from electrons to atoms and ions.

The species taken into account in our model, for Ar gas and Cu as sample material, include the Ar atoms, Ar^+ and Ar^{2+} ions, the Cu atoms, Cu^+ and Cu^{2+} ions, as well as the electrons.

The operating conditions, sample characteristics and geometrical parameters for which calculation results will be shown in Section 4, are listed in Table 1.

3.2. Equations to be solved in the model

The gas flow dynamics are calculated assuming laminar flow conditions, by solving conservation equations for mass and momentum (*i.e.*, Navier–Stokes equation) for all gas flows. For flows involving heat transfer (as is the case in our model), an additional equation for energy conservation is also solved. Furthermore, the local mass fraction of a species is calculated with a transport-diffusion equation. These conservation equations also contain source and loss terms. The source term for the mass conservation equation is the mass added to the continuous phase (*i.e.*, gas phase) from the discontinuous phase (*i.e.*, due to evaporation of the liquid droplets; see below). The Lorentz force is the source term in the momentum equation, while the energy conservation equation has both a source and a loss term, given by the electric power density and the emitted radiation, respectively. These source and loss terms are calculated by self-written codes and loaded in FLUENT as user defined functions (UDFs). The power density is calculated by Ohm's law. Note that this power density needs to be adapted during the calculations. Indeed, this calculated power density should not exceed the input power density, because the generator will not deliver more power, but it is well possible that less power is coupled into the plasma. To account for this, the electric current, which defines the electric field, is adapted. This loop to update the current, electric field and coupled power density, is illustrated by the red arrow in Fig. 2 below.

The electromagnetic field is also calculated in a self-written code, based on the Maxwell equations, and loaded as user defined scalars (UDS) in FLUENT. Moreover, the material parameters, *i.e.*, the viscosity of the mixture (consisting of various heavy species, such as the atoms and ions of both the gas and the sample material, as well as the electrons), the heat capacity, thermal conductivity and diffusion coefficients of the species are also defined in the model as UDFs, being a function of the actual gas composition and the plasma temperature.

Since we assume that the ICP is in LTE, the ionization is described by the Saha-Eggert equation. Furthermore, based on the assumptions of quasi-neutrality and conservation of heavy species, in combination with the calculated ionization degree, the number densities of all species, *i.e.*, atoms and (singly and doubly charged) ions of Ar and of the Cu sample material (see below), as well as the electrons, can be calculated, again by UDFs, *i.e.* self-written codes.

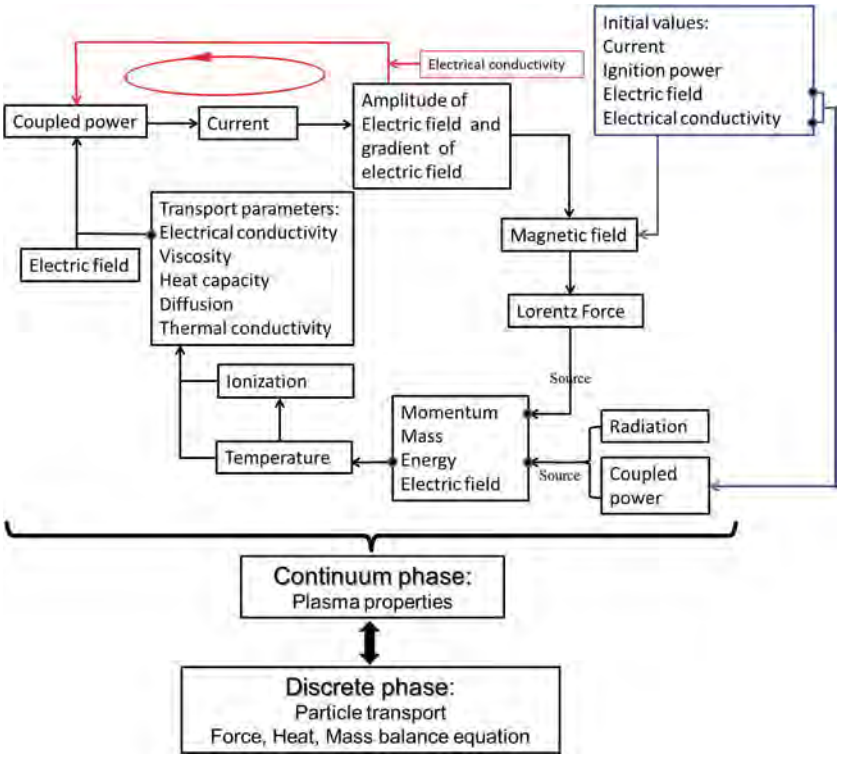

Fig. 2 Flowchart, showing the solution strategy of the model.

The sample introduction is described with the so-called "discrete phase model (DPM)".[134] As mentioned above, Cu is taken as case study in our model, and we introduce it as elemental particles. In fact, we calculate the transport properties of the particles based on the actual temperature of the Ar flow. Hence, they are carried with the transport properties of first solid (300–1357 K) and then liquid phase (>1357 K), up to reaching the vaporization point. Note that we do not include the melting process, because this is not possible in the DPM as it can only treat elemental sample particles in liquid phase. This approximation is justified, because the latent heat of melting for Cu (203.5 kJ kg^{-1}) is much smaller than the latent heat of vaporization (5310 kJ kg^{-1}),[135] and melting can thus be ignored in our calculations.

We calculate the trajectory of each particle by means of the Newton equation (*i.e.*, so-called force balance). The main force is the drag force, being a function of the molecular viscosity of the fluid, the mass density and diameter of the particles. We apply in our model a variation of the Stokes drag law, including the so-called Cunningham correction factor,[136] and we also take the effect of Brownian motion into account.

Besides the particle transport throughout the ICP, we also describe the heating and evaporation of the particles, as well as the ionization of the vapor atoms. At this stage we assume purely elemental particles, which is mostly relevant for LA-ICP-MS. In the future, we plan to extend our model to aerosol particles, but this will be more complicated, because also the desolvation and chemical reactions between the elements and the water molecules will have to be accounted for.

We describe the heating of the particles by means of a heat and mass balance equation, which relates the particle temperature to the convective and diffusive heat transfer. Furthermore, we calculate the mass transfer from the liquid to the vapor phase by means of an evaporation and boiling rate based on thermodynamic relations, accounting for both surface evaporation and convective boiling, respectively.[136–138] Note that the heat lost or gained by the particle as it traverses each computational cell will also appear as a source or sink of heat, respectively, in the subsequent calculation of the continuous phase energy equation, describing the vapor phase. Once the sample material is in the vapor phase, we treat the individual atoms in the same way as for the carrier gas, by solving the conservation equations of mass, momentum and energy, and the Saha-Eggert equation to calculate the ionization degree of the sample material at the local plasma temperature, assuming LTE. Subsequently, as mentioned above, we can calculate the number densities of electrons and of the atoms and ions of the sample material, based on the ionization degree and the (mass and charge) conservation equations, like for Ar.

We need several material parameters for the sample material, both in liquid phase and in gas phase. The parameters for the particles are mainly taken from ref. 135. The viscosity, thermal conductivity and diffusion coefficients are again inserted in the model as UDFs, like for Ar, as they are a function of the local gas composition and plasma temperature. The diffusion coefficient of Cu particles in Ar gas as a function of temperature is adopted from ref. 139.

3.3. Calculation strategy

The whole simulation setup is divided in three major steps. The first step, *i.e.*, pre-processing step, includes the preparation of the geometry and mesh, providing the physical equations or properties as UDFs and UDSs, as well as defining the boundary and initial conditions. In the second step the model is solved, while the third step accounts for the post-processing or analyzing the results.

The solution strategy of the model is depicted in Fig. 2. The ignition power creates a current density and an electric field. Subsequently, the magnetic field is calculated from the spatial derivative of the electric field. From the electromagnetic fields, the Lorentz force density is obtained. Next, the three conservation equations of mass, momentum and energy are solved (including the source terms) and the electric field is calculated (as a UDS). This provides among others the gas flow velocities and the plasma temperature. Based on the latter, and assuming LTE, the Saha-Eggert equation is solved, to provide the number density of ions and electrons. The transport parameters (*i.e.*, electrical conductivity, viscosity, heat capacity, diffusion and thermal conductivity) are calculated based on the temperature and number density of the species. From the electric field and electrical conductivity, a new value for the power is reached for each cell. By integrating this power over the entire volume in which the power is coupled, we can calculate the total coupled power. At this point, we need to check whether the total calculated power exceeds the input power or not. If yes, we need to update the current and the electric field, as indicated by the red circle in Fig. 2, and this procedure needs to be repeated until the power becomes lower than or equal to the input power. Subsequently, the magnetic field can be updated, as well as the rest of the equations.

To implement the DPM into the rest of the ICP-MS model, we first build a FLUENT model accounting for the injection properties, material parameters and the physical models applicable to the elemental particles, *i.e.* transport, heating, vaporization, boiling and ionization, as well as the particle transport UDFs. In our solution strategy, we first obtain stable plasma properties for Ar in the so-called continuous phase model (CPM), *i.e.* for the plasma temperature and electron density and for the gas flow behavior. Subsequently, we introduce the Cu particles into the ICP with the DPM, and we combine the calculation in the CPM with the DPM until convergence is reached. During each iteration, we calculate the exchange of mass, momentum and energy between plasma and particles, and we update the DPM and CPM. Finally, after convergence is reached, we can track the particles to determine their position, their phase (liquid or vapor), velocity and temperature, as well as the ionization of the vapor atoms.

Note that the model describes the injected material transport up to the sampling cone, but the rest of the ion transport inside the MS is not yet accounted for in our current model.

3.4. Validation of the model with experiments

When the model was initially developed, we made a comparison between the modeling results and experimental measurements for the plasma temperature and gas flow velocity, for a range of different injector gas flow rates, to validate the model.[126] Furthermore, the modeling results obtained at later stages, at various conditions, are also compared with experimental data from literature as much as possible, as will be outlined in Section 4 below.

The plasma temperature inside the central channel was measured from the end-on collected line-to-background ratio.[126] As can be observed from Fig. 3, the calculated and measured values for the plasma temperature are in good agreement (*i.e.*, within 3% deviation) in the range of injector gas flow rates relevant for the analysis of relatively large particles, *i.e.*, ~50 μm. The deviation increases for higher injector gas flow rates, but stays below 6% for all flow rates investigated.

We also compared the calculated and measured gas velocities as a function of injector gas flow rate,[126] as illustrated in Fig. 4. The gas velocity inside the coil region was experimentally determined by side-on analyte emission measurements with single monodisperse droplet introduction, while in the simulations it was obtained from the injector gas path lines. As shown in Fig. 4, the gas velocity in the region between the first and second winding of the coil (indicated as "path 1") is significantly lower than in the region between the second and third winding (indicated as "path 2"), both in the calculated and measured results. The deviation between calculated and measured data is quite significant in the first region, and can be attributed to the fact that the methods used for velocity determination in the calculations and the experiments are not fully consistent (see ref. 126 for more details). Note that the investigated flow rates in this region were limited to low values, because the experiments did not produce proper signals at higher flow rates. However, in the second region the calculated and measured velocity values are in excellent agreement.

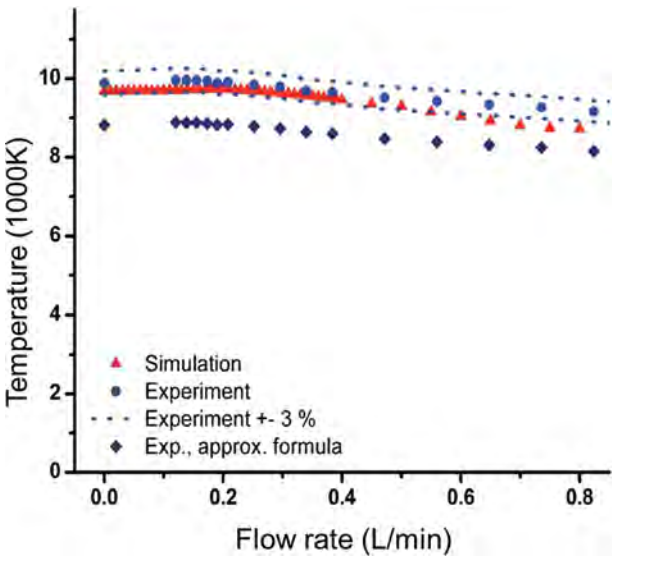

Fig. 3 Calculated and measured plasma temperatures as a function of injector gas flow rate. Reprinted with permission from ref. 126. Copyright 2011 American Chemical Society.

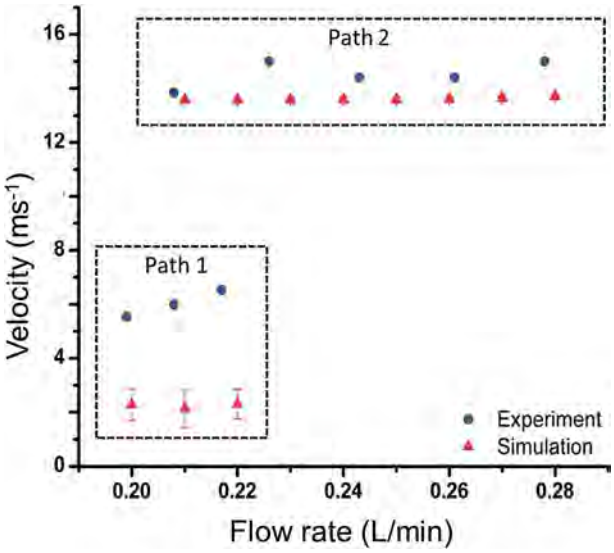

Fig. 4 Calculated and measured velocities as a function of injector gas flow rate, for two different regions inside the ICP, *i.e.*, path 1 corresponds to the region between the first and second winding of the coil, whereas path 2 corresponds to the region between the second and third winding of the coil. Reprinted with permission from ref. 126. Copyright 2011 American Chemical Society.

4. Typical results obtained by the modeling

The model provides information about characteristic features in the plasma, such as the gas flow patterns, the plasma temperature and the electron density, as well as about the sample behavior, including transport, evaporation and ionization. In the next two sections, we will first show the general ICP characteristics and sample behavior at typical gas flow rates (*i.e.*, 1 L min^{-1} injector gas, 0.4 L min^{-1} auxiliary gas, and 12 L min^{-1} outer gas flow rate), a plasma power of 1000 W, and Cu particles of 1 μm diameter, injected at a mass loading flow rate of 100 ng s^{-1}. Furthermore, the diameters of the injector inlet and sampler orifice are kept fixed at 1.5 mm and 1 mm, respectively, and the sampling cone is positioned 10 mm from the load coil. The other parameters are listed in Table 1 above. In the later sections, we will present the effect of the presence of a sampling cone, the sampler orifice diameter and position, the injector inlet diameter and position of particle injection, the gas flow rates and plasma power, as well as the particle diameter and particle loading flow rate, on the ICP characteristics and on the behavior of the sample material.

4.1. General ICP characteristics: plasma temperature and electron density profiles, and gas flow behavior

Fig. 5 illustrates the 2D profiles of the calculated plasma temperature, electron number density and of the gas flow velocity path lines, for the conditions mentioned above. The plasma temperature profile is characterized by a maximum (of about 10 000 K) near the coils, with a cool central channel.

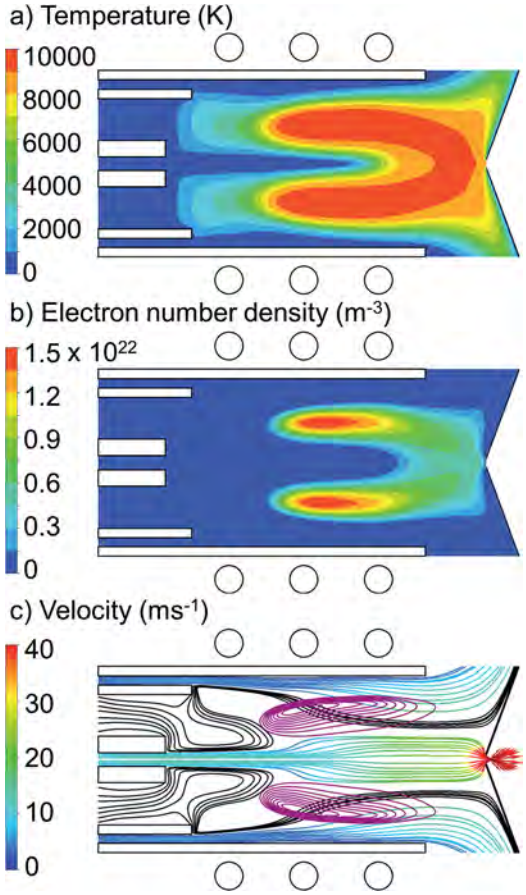

Fig. 5 2D profiles of the plasma temperature (a), electron density (b) and the gas flow velocity path lines (c), calculated for 1 L min^{-1} injector gas, 0.4 L min^{-1} auxiliary gas, and 12 L min^{-1} outer gas flow rate, and a plasma power of 1000 W. The diameters of the injector inlet and sampler orifice are 1.5 and 1 mm, respectively. The sampling cone is placed 10 mm from the load coil. Note that the color scale in panel (c) indicates the gas velocity for the injector gas and outer gas, while the auxiliary gas flow path lines are colored in black, to distinguish them from the injector gas and outer gas. The purple contours in panel (c) indicate the region of maximum power coupling.

Hence, the electron number density also reaches its maximum (in the order of 10^{22} m^{-3}) in this region, due to the higher ionization degree at higher temperature. Thus, the intense plasma is very localized, with a toroidal shape.

The gas flow path lines are plotted in Fig. 5(c). Note that only the path lines of the injector gas and outer gas are indicated in color, while the auxiliary gas flow path lines are colored in black, to distinguish them from the injector gas and outer gas path lines. The injector gas goes more or less straight towards the sampling cone at these conditions, with little expansion, and has typical velocities between 10 and 30 m s^{-1}, increasing at the sampling cone towards 100 m s^{-1} and above. As will be shown below, this flow pattern can be different at other conditions. The auxiliary gas has slightly lower velocities (in the order of 5–25 m s^{-1}), and is characterized by backward motion (so-called recirculation). The latter is also affected by the discharge conditions, as will be shown below. At the conditions

illustrated here, all the auxiliary gas exits through the open ends of the ICP torch, and it passes through the region of maximum power coupling (indicated by the purple contours in Fig. 5(c)), which is beneficial for efficient heat transfer. However, also this behavior depends on the discharge conditions, as will be shown below. Finally, the outer gas has velocities in the order of 5–10 m s^{-1}.

4.2. Behavior of sample particles in the ICP: transport, evaporation, ionization

To illustrate the behavior of the Cu particles in the ICP, as well as their effect on the plasma characteristics, we introduce Cu particles from the injector gas inlet with 1.5 mm diameter and we follow them throughout the ICP up to the sampler position (*i.e.* 41.5 mm distance from the injector gas inlet), for the same applied power and gas flow rates as mentioned above. Furthermore, we assume a Cu mass loading flow rate of 100 ng s^{-1} and a particle diameter of 1 μm, as also stated above. This value of the mass loading flow rate is based on LA studies and taken from experimental values of fs-LA of Cu cells for a long washout time.[140]

Fig. 6(a) illustrates the 2D trajectories of the injected Cu particles, colored according to their temperature. The Ar gas flow path lines from the injector gas, auxiliary gas and outer gas are also plotted, colored in black, to indicate the path lines which the Cu particles can follow. The particles enter the ICP at room temperature, as mentioned in Section 3.2 above, and they are gradually heated until they reach the evaporation temperature (=1850 K) and finally boiling temperature (=2830 K). Once they are evaporated, they disappear from the particle path lines, and we trace them further in the gas phase domain.

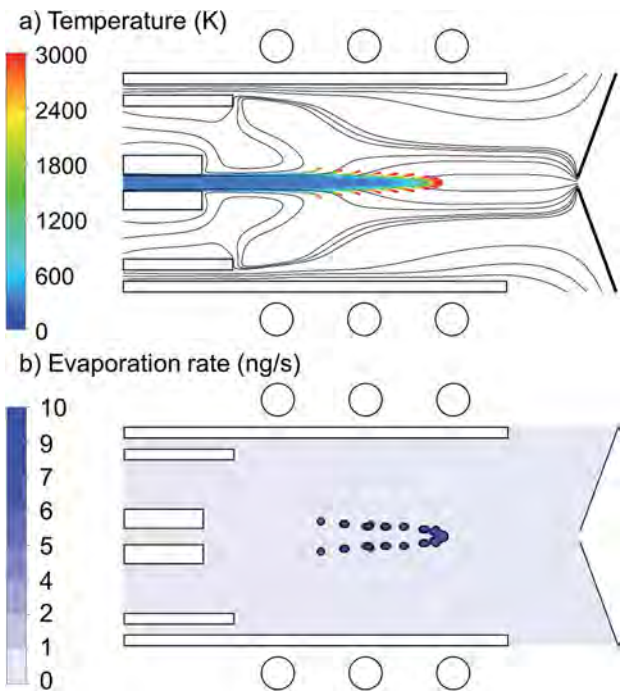

Fig. 6 2D trajectories of injected Cu particles, colored according to temperature, until they are evaporated, as well as the path lines of the injector gas, auxiliary gas and outer gas, colored in black (a), and 2D distribution of the Cu evaporation rate (b), for Cu particles with diameter of 1 μm and mass loading flow rate of 100 ng s^{-1} injected from the injector gas inlet. The other conditions are the same as in Fig. 5.

The 2D evaporation rate of the Cu sample is depicted in Fig. 6(b). Looking at both Fig. 6(a) and (b), it is clear that the particles, which are all injected from the injector gas inlet, are not evaporated at the same position in the ICP. The reason is that the particles follow the Ar gas flow path lines, and it is obvious from Fig. 6(a) that not all of the injector gas flows in a straight line to the sampler, but is subject to some expansion in the radial direction, as also observed in Fig. 5(c) above. Due to this radial expansion of the injector gas, some gas path lines reach the higher temperature regions in the torch earlier in space (*cf.* Fig. 5(a) above). Hence, the particles following these path lines start to evaporate at earlier positions, while the particles following the inner gas path lines stay longer at the central axis, *i.e.*, the cool channel, so they evaporate at later positions.

Besides, it is reported in literature that the analyte atoms will diffuse and become ionized, forming ion vapor clouds with increasing diameter downstream the plasma.[58,141] Note that due to the early evaporation and more radial expansion from the central axis, a fraction of the sample ions may not reach the sampler orifice, which will cause a loss in signal, as also discussed by Niemax.[58] Alternatively, even if the sample ions are not lost, the radial expansion will result in a delay in detection time, as discussed by Borovinskaya *et al.*[62] The exact position of injection has a significant effect on the radial expansion from the central axis, and thus on the evaporation position. This will be discussed in more detail in Section 4.5 below.

Once the Cu particles are evaporated, the Cu vapor atoms are subject to ionization. Fig. 7 illustrates the 2D number density profiles of the Ar atoms, Ar^+ and Ar^{2+} ions (left column; a–c), and of the Cu atoms, Cu^+ and Cu^{2+} ions (right column; d–f) for the same conditions as above. Note that the scales of these density profiles are different, in order to clearly show where are the maximum values for each species.

The Ar gas atoms are by far the most abundant, with a number density of 2.4×10^{25} m^{-3} (*i.e.*, corresponding to atmospheric pressure and room temperature) when entering the ICP, but this value drops to around 6×10^{23} m^{-3} inside the plasma, due to the high temperature, giving rise to ionization. It is clear that Ar is mainly ionized in the coil region, at the position of maximum power deposition (see purple contours in Fig. 5(c) above) and maximum temperature (see Fig. 5(a) above). The Ar^+ ion number density has a maximum of 1.5×10^{22} m^{-3}, while the maximum Ar^{2+} ion number density is slightly below 10^{14} m^{-3}, hence 8 orders of magnitude lower than the maximum Ar^+ ion number density. In other words, a negligible fraction of the Ar^+ ions is further ionized into Ar^{2+} ions, which is like expected, given the high second ionization potential of Ar (*i.e.*, 27.7 eV). From the volume integrated densities over the entire torch, we can deduce that the ionization degree of Ar is about 0.027%.

The Cu atoms are characterized by a maximum number density at the location of maximum evaporation (*cf.* Fig. 6(b)

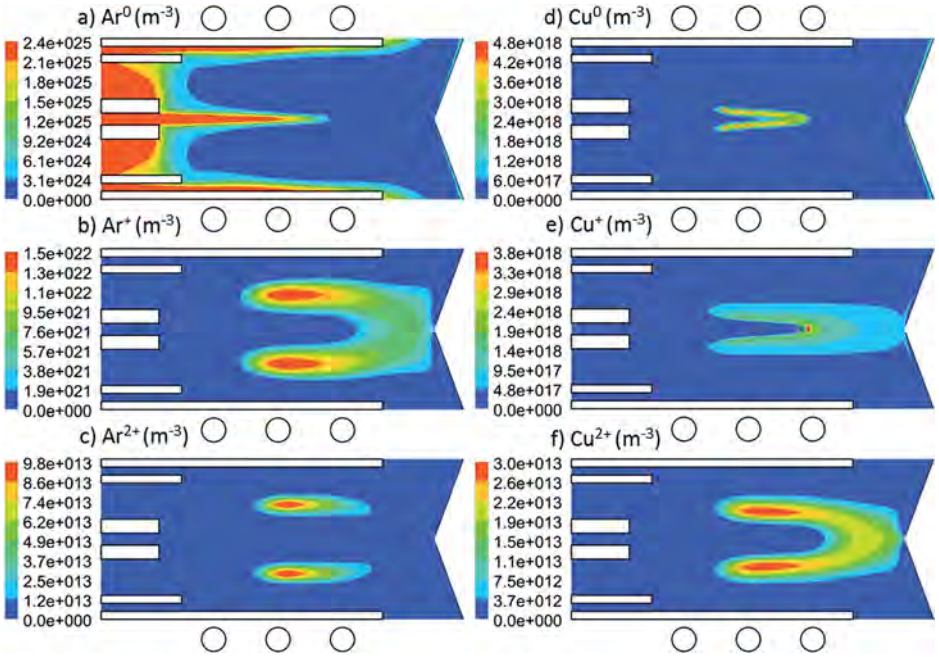

Fig. 7 2D number density profiles of the various species in the ICP: Ar^0 (a), Ar^+ (b), Ar^{2+} (c), Cu^0 (d), Cu^+ (e) and Cu^{2+} (f), for Cu particles with diameter of 1 μm and mass loading flow rate of 100 ng s^{-1} injected from the injector gas inlet. The other conditions are the same as in Fig. 5.

above), which is logical. Integrated over the entire ICP torch, the Cu atom density is more than 7 orders of magnitude lower than the Ar gas atom density, at the Cu mass loading flow rate illustrated here (*i.e.*, 100 ng s^{-1}). The Cu^+ ions reach a maximum at the central axis, at the position of maximum evaporation and where the plasma temperature starts rising (*cf.* Fig. 5(a) above). The Cu^{2+} ions reach their maximum in the region of maximum temperature, like in the case of Ar. Furthermore, the density of the Cu^+ and Cu^{2+} ions is still appreciable near the sampler. The overall ionization degree of Cu, integrated over the entire ICP, is about 60%, which is much higher than for Ar. This is explained by the lower ionization potential of Cu (*i.e.*, 7.73 eV *vs.* 15.76 eV for Ar). Only a small fraction (*i.e.*, about 0.001%) of the Cu^+ ions is further ionized into Cu^{2+} ions. This fraction, although being very low, is still much higher than for Ar, which is again explained by the lower second ionization potential of Cu (*i.e.*, 20.9 eV *vs.* 27.7 eV for Ar).

In summary, Fig. 7 gives an indication to what extent the clouds of each species expand in the torch, which is useful for both optical emission and mass spectrometry. In the framework of ICP-MS, we are especially interested in the fluxes of the various species at the position of the sampler orifice, and more specifically in the fraction of Cu^+ ions arriving at the sample orifice, with respect to the amount of Cu injected in the ICP. This fraction, which is a measure of the Cu sample transport efficiency from the injector gas inlet towards Cu^+ ions entering the MS through the sampler orifice, turns out to be about 42% for the conditions under study here, but it depends on the operating conditions, and especially on the injection position in the injector gas inlet. This will be discussed in more detail in Section 4.5 below.

The plasma temperature calculated upon including the Cu particles in the model is exactly the same as the result without incorporating these Cu particles (*cf.* Fig. 5(a)). Hence, we can conclude that the sample introduction does not affect the plasma temperature, at least for the Cu mass loading flow rate of 100 ng s^{-1}.[132] This is not unexpected, because the latter is 10 orders of magnitude lower than the Ar flow rate. In fact, only when we would increase the Cu mass loading flow rate to the order of 500 μg s^{-1}, some cooling effect due to the evaporation of the sample particles can be observed, as will be discussed in detail in Section 4.9 below.

4.3. Effect of the presence of the sampling cone

Fig. 8 illustrates the effect of the presence of the sampling cone, or interface towards the MS, on the calculated gas flow velocities, for the same conditions as in Fig. 5. It is clear that the plasma velocity rises dramatically in the region close to the sampling cone, from an average value of about 20 m s^{-1} to a value above 100 m s^{-1} when the gas passes the sampling cone. This is attributed to the pressure drop behind the sampling cone. Furthermore, the cool metal interface lowers the plasma temperature and hence also the electron density very close to the sampling cone, while the plasma temperature and electron density inside the coil region are somewhat higher. This was illustrated in detail in ref. 127. The reason is that the auxiliary gas passes better through the region of maximum power coupling in case of the presence of the sampling cone, as shown in Fig. 8. The latter results in more efficient gas heating, yielding a somewhat higher plasma temperature in the coil region, and thus also a slightly higher electron density. Thus, we can conclude that the effect of the sampling cone on the plasma characteristics strongly depends on the measurement position. We have demonstrated that even a small shift from the actual

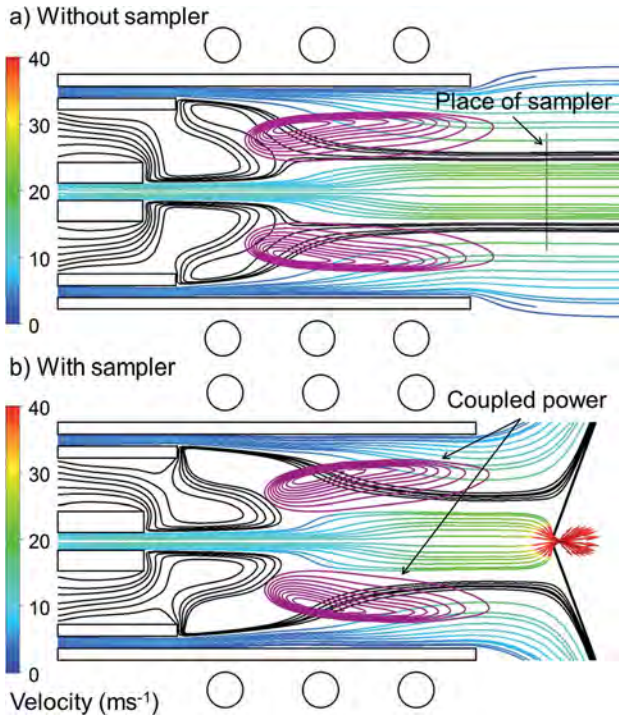

Fig. 8 2D gas flow velocity path lines, without (a) and with (b) sampling cone, for the same conditions as in Fig. 5. Again, the color scale indicates the gas velocity for the injector gas and outer gas (in m s^{-1}), while the auxiliary gas flow path lines are colored in black, and the purple contours indicate the region of maximum power coupling.

position of the sampler (*cf.* the vertical lines in Fig. 8(a)) can significantly affect the measurement result.[127] Our calculation results on the effect of the sampling cone are in good qualitative agreement with experimental data from the groups of Farnsworth, Olesik and Hieftje.[9,20,21]

4.4. Effect of sampling cone orifice diameter and position

In Fig. 9, the plasma temperature and gas flow path lines are plotted for a sampler orifice diameter of 1 mm and 2 mm, at the same conditions as in Fig. 5. Close to the sampler, the temperature is slightly higher in case of the larger orifice diameter, because the cooling effect is less pronounced, but in the rest of the plasma, the effect is negligible. The same is true for the effect on the electron density.[129]

On the other hand, the effect is more pronounced for the gas flow path lines, especially for the auxiliary gas, as is clear from Fig. 9. More specifically, the backward motion (recirculation) of the auxiliary gas is reduced in case of a larger sampler orifice diameter. The reason is that the auxiliary gas is "sucked" into the MS, which reduces its backward motion. Furthermore, because there is less interaction between the gas atoms and the sampling cone in case of the larger sampler orifice diameter, this results in more efficient gas transfer through the sampler.[129] On the other hand, the flow velocity at the sampler position turns out to be independent from the sampler orifice diameter.[129]

It is also clear from Fig. 9 that, by changing the sampler orifice diameter, we can control whether only the injector gas or also (part of) the auxiliary gas can pass through the sampler orifice. Indeed, for the conditions presented here (*i.e.*, injector inlet diameter of 1.5 mm), only the injector gas can pass through the sampler orifice in case of the 1 mm sampler orifice diameter, whereas in case of the 2 mm sampler orifice diameter, some part of the auxiliary gas can also pass through the sampler orifice, as is obvious from Fig. 9. Depending on the size of the sample ion cloud, one or the other situation might be beneficial. If the sample ion cloud is small, so that it is only transported by the injector gas, the first situation is beneficial, but in case when the sample ion cloud is larger, part of it will be transported by the auxiliary gas, and then, the second situation might be desired.

We have also investigated the effect of the position of the sampling cone, by varying the distance from the load coil between 7 and 17 mm.[129] Our calculations reveal that a larger distance between load coil and sampling cone yields a slightly lower plasma temperature at the position of the sampler, as expected, and this might have consequences for the ion generation and transport through the sampling cone. More details about the effect of the sampler orifice diameter and position can be found in ref. 129.

4.5. Effect of the injector inlet diameter and of the Cu particle injection position

Fig. 10 illustrates the gas flow path lines for an injector inlet diameter of 1.5 mm and 2 mm. At 1.5 mm injector inlet

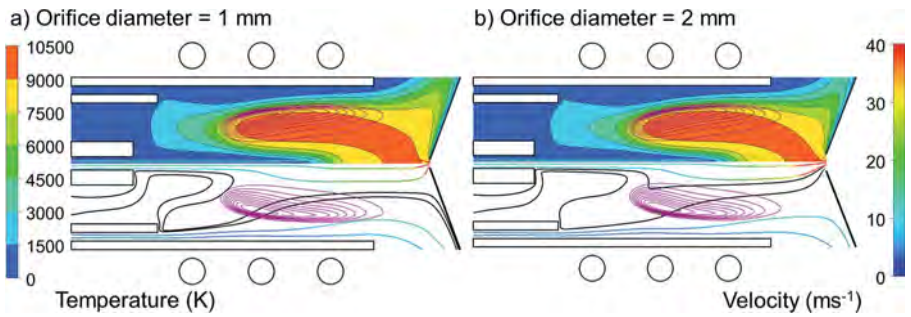

Fig. 9 2D plasma temperature profiles (upper frames) and gas velocity path lines (lower frames) for a sampler orifice diameter of 1 mm (left panel) and 2 mm (right panel). The other conditions are the same as in Fig. 5. The color scale indicates the gas velocity for the injector gas and outer gas, while the auxiliary gas flow path lines are colored in black, and the purple contours indicate the region of maximum power coupling. Reproduced from ref. 129 with permission from the Royal Society of Chemistry.

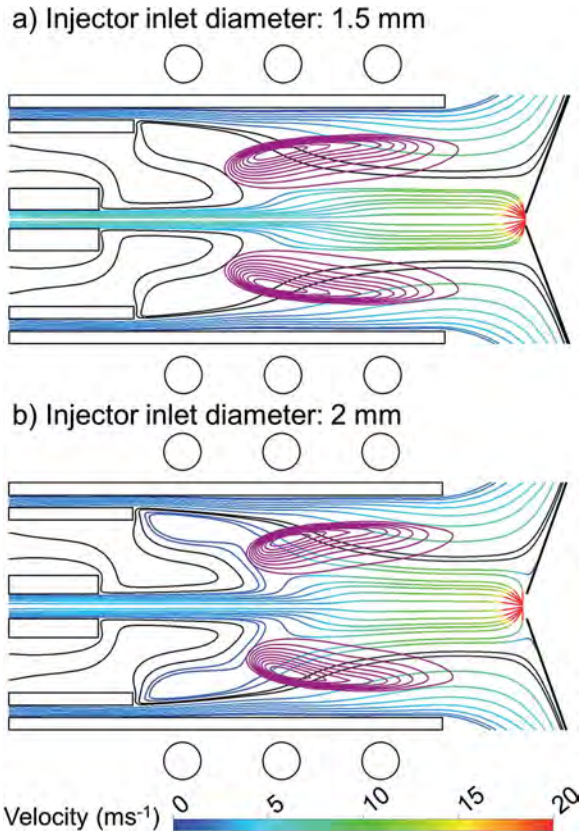

Fig. 10 2D gas flow velocity path lines for an injector inlet diameter of 1.5 mm (a) and 2.0 mm (b). The other conditions are the same as in Fig. 5. Again, the color scale indicates the gas velocity for the injector gas and outer gas, while the auxiliary gas flow path lines are colored in black, and the purple contours indicate the region of maximum power coupling. Reproduced from ref. 130 with permission from the Royal Society of Chemistry.

diameter, the injector gas goes in a (more or less) straight line towards the sampling cone, while at 2 mm injector inlet diameter, a fraction of the injector gas exhibits backward motion (recirculation). This recirculation behavior is observed in both cases for the auxiliary gas, and was also illustrated in Fig. 5(c), 8 and 9 above, but for the injector gas, it only happens in case of the larger injector inlet diameter. It is obvious that this recirculation of the injector gas should be avoided, as it reduces the sample transport efficiency through the sampling cone. Indeed, as is clear from Fig. 10(b), a certain fraction of the injector gas will not be able to pass through the sampler orifice, but will leave the ICP through the open ends, leading to signal loss.

Furthermore, this recirculation behavior in the injector gas flow path lines can explain the very long analytical signals found in experiments at low gas flow rates. In previous work, we carried out simulations for different injector inlet diameters between 0.5 and 2.5 mm, to elucidate which conditions yield good analyte transport and optimum signals.[126] According to these model predictions, there exists a transition flow rate for each different injector inlet diameter, which indicates the lower limit for effective analyte transport conditions throughout the plasma. Note that this transition flow rate is not the optimum flow rate for analysis; the latter will be somewhat higher. The transition flow rate, and thus also the optimum flow rate, increases upon rising injector inlet diameter. The simulations also allowed to define a rule-of-thumb equation, to estimate the transition flow rate for a given injector inlet diameter as well as injector gas composition (argon/helium mixture). More details about this study can be found in ref. 126.

We also investigated the effect of the Cu particle injection position on the Cu particle transport, for an injector inlet diameter of 1.5 mm. For this purpose, we introduced 5 different Cu particles of 1 μm diameter, with flow rate of 100 ng s^{-1}, from different initial radial positions at the injector gas inlet, and we followed their trajectory until evaporation within the ICP. In Fig. 11, the radial positions of these 5 particles, as long as they are in the liquid (or solid) phase, are plotted as a function of their axial position in the ICP, illustrating their trajectory. Their starting positions at the injector inlet are schematically indicated in the top right of the figure, and the axial position of the load coils is also presented for the sake of clarity. It is obvious that each particle follows a different trajectory when entering from a different initial position. Most apparent is that the radial expansion of the outermost particle (particle 5) starts earlier in space than for the other particles, while particle 1, which is injected on-axis, follows a straight path line at the central axis, until it is vaporized. This can be explained from the Ar gas path lines, illustrated *e.g.*, in Fig. 5(c) above. Indeed, the central Ar gas path line moves in a perfect straight line on-axis, while the other path lines show some radial expansion.

As mentioned above, a deviation from the central axis will lead to a longer transit time and a loss of intensity. Moreover, when the sample particles move in the radial direction, this lowers the chance that the sample can leave the plasma through the sampler cone, so the detection efficiency will become lower, as some part of the sample will be lost in the ICP. Moreover, even if all the analyte can pass through the sampler cone, any

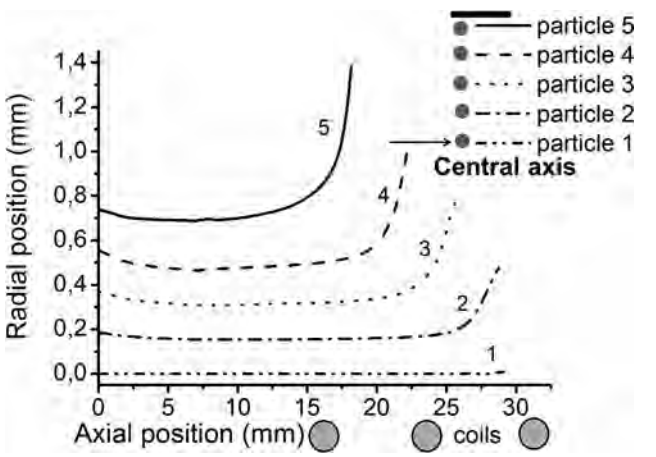

Fig. 11 Radial position of 5 different Cu particles (with different injection positions; see legend) as a function of their axial position in the ICP, to illustrate the effect of their injection position on their trajectory. The conditions are the same as in Fig. 5 and 6. The positions of the load coils are also indicated in the figure, for clarity.

deviation from the central axis will affect the transmission between the first and second vacuum stage of the MS. This was studied by Farnsworth and Spencer, who reported that gas flows passing through the sampling cone off-axis, will expand off-axis in the first vacuum stage and therefore get lost in the skimming process.[32,123,124,142–144] Furthermore, Perdian *et al.* illustrated, when studying the effect of particle size on the ICP-MS signals, that the exact influence of large particles on the signal also depends on their position in the ICP.[53] Such effects are exacerbated by the fact that the ICP-MS signal basically reflects the composition of the plasma in a region with diameter equal to the skimmer diameter just in front of the sampler.[122] Thus, if the particle is displaced off-axis through the sampler and skimmer, its M^+ vapor cloud is also off-axis, and it mainly contributes to the steady state signal. On the other hand, if the large particle is on-axis and is still intact as it approaches the sampler, the excess M^+ ions surrounding the intact particle generate a large positive increase in the M^+ signal, but only for a brief time, comparable to the flight time of the particle through the ICP.[53]

We recently studied in more detail the effect of the Cu particle injection position, by comparing different injector inlet diameters, as well as on-axis and off-axis injection.[132] It was very clear that when the Cu particles are injected on-axis, they stay on-axis throughout the ICP until they become evaporated. On the other hand, the wider the area of particle injection, the more radial expansion occurs for the particles, as well as for the vapor cloud. Thus we can conclude that the position of vapor production in both the axial and radial direction depends strongly on the exact initial injection position.

Fig. 12 illustrates the 2D Cu^+ ion number density profiles for on-axis injection (more specifically within 0.25 mm width from the center of the inlet; upper frame) and off-axis injection (*i.e.*, within 0.25 mm from the side wall of the inlet; bottom frame). The trajectory of the Cu particles is plotted in brown path lines. Only one half part of the ICP torch is shown for both cases, to allow easy comparison. As also illustrated in Fig. 11, the particles that are injected on-axis move in a straight line at the central axis, whereas the particles that are injected off-axis deviate to some extent from the central axis (*cf.* upper and bottom frame in Fig. 12). As a result, the ion cloud in case of the on-axis injection is concentrated near the central axis, whereas the ion cloud in case of off-axis injection has a much broader profile, with its maximum reached earlier in space.

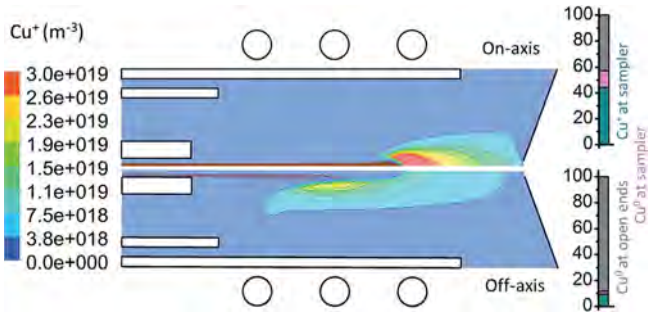

Fig. 12 2D Cu^+ ion number density profiles for on-axis (upper frame) and off-axis (bottom frame) injection, as well as trajectory of the Cu particles (brown path lines). At the right of the figure, the fraction of Cu^+ and Cu^0 at the sampler and fraction of Cu^0 leaving at the open ends of the ICP, with respect to the total amount of Cu at the inlet, for both on-axis and off-axis injection, are plotted. The other conditions are specified in Fig. 5 and 6.

At the right-hand side of Fig. 12, we compare the fractions of Cu^0 atoms and Cu^+ ions passing through the sampling cone, as well as the fraction of Cu^0 atoms leaving the ICP through the open ends, for both on-axis and off-axis injection. The fractions of Cu^{2+} ions are negligible in both cases, and therefore not shown. Obviously, only the fraction of Cu^+ ions passing through the sampling cone is relevant for the ICP-MS signal, as Cu^0 would not be detected in the MS. This fraction is calculated from the flux of Cu^+ ions passing through the sampler (by integrating over the entire orifice width) compared to the Cu particle flux entering the ICP at the injector gas inlet. Hence, this fraction indicates the transport efficiency of the sample material from the inlet till entering the MS interface as Cu^+ ions.

In case of on-axis injection, this transport efficiency is about 44%, while about 13% of the material passes as Cu^0 atoms through the sampler, and 43% leaves the ICP through the open ends. In case of off-axis injection, on the other hand, only 10% of the injected material will pass through the sampling cone as Cu^+ ions, while about 2% passes as Cu^0 atoms and 88% leaves the ICP through the open ends. Hence, this clearly illustrates the significant effect of injection position on the transport efficiency of Cu^+ ions through the sampler, and thus most probably also on the ICP-MS signal (although the latter is not calculated in our model).

In general it is clear that the radial movement of the sample particles to the outer region of the ICP will lower the chance that the sample can pass through the sampling cone. This suggests that using smaller injector inlets will be beneficial. The latter was indeed observed experimentally in ref. 58. For larger injector inlets, like 2 mm diameter, the transport efficiency is only good for on-axis injection, where we calculated a value around 90% in our recent paper.[133] However, for LA applications, the exact particle injection position is difficult to control, so for this reason, we believe that smaller injector inlets are beneficial, as is indeed most often used for LA applications.[53,56,61]

4.6. Effect of the gas flow rates

The values of the injector gas, auxiliary gas and outer gas flow rates largely affect the gas flow patterns and other plasma characteristics inside the ICP. In Fig. 13 we plot the calculated plasma temperature profiles for different values of the injector gas flow rate, at fixed values of the auxiliary gas flow rate (0.4 L min^{-1}) and outer gas flow rate (12 L min^{-1}).[128] The input power is fixed at 1000 W and the injector inlet diameter and sampler orifice diameter are 1.5 mm and 1 mm, respectively, as mentioned above.

The plasma temperature clearly drops upon higher injector gas flow rate, and the cool central channel becomes more pronounced. There is almost no central channel at a flow rate of 0.3 L min^{-1}, while at 1.4 L min^{-1}, the cool central channel

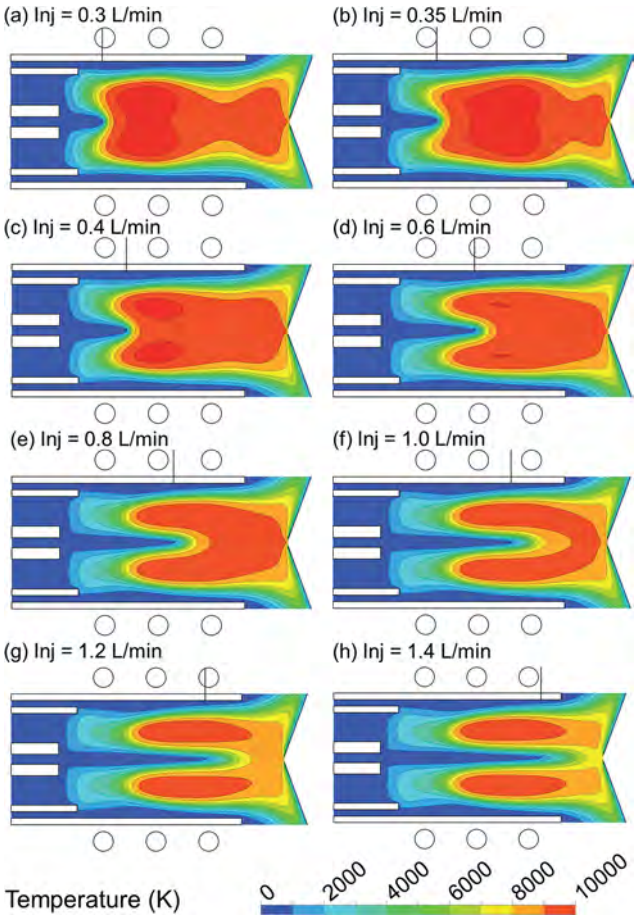

Fig. 13 2D plasma temperature profiles (K), at different values of the injector gas flow rate, ranging from 0.3 to 1.4 L min^{-1}. The other conditions are the same as in Fig. 5. The small black lines above each plot indicate the length of the cool central channel. Reprinted from ref. 128 with permission from Elsevier.

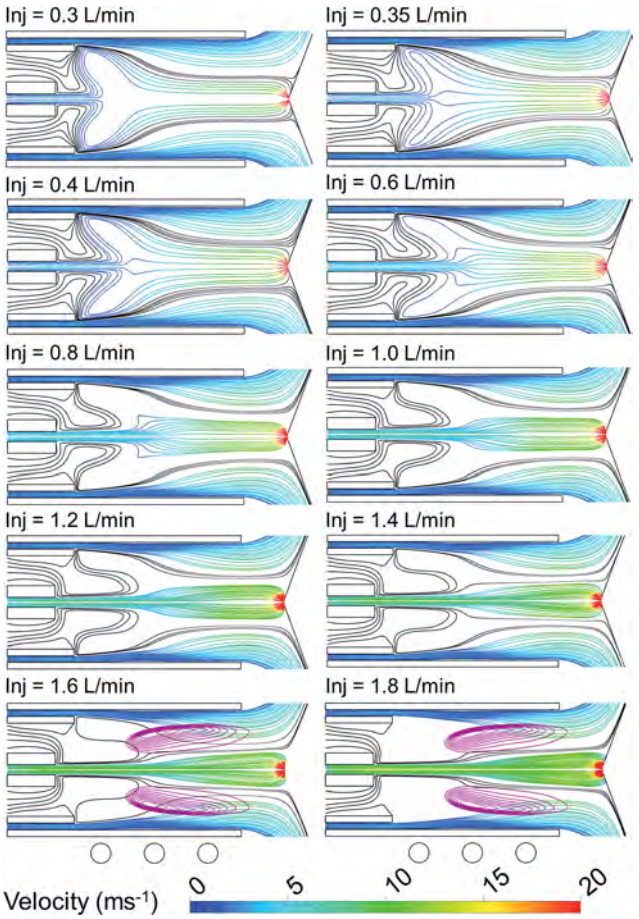

Fig. 14 2D gas flow velocity path lines originating from the injector gas and outer gas inlets, colored by velocity in m s^{-1}, and from the auxiliary inlet, colored in black, at different values of the injector gas flow rate, ranging from 0.3 to 1.8 L min^{-1}. The other conditions are the same as in Fig. 5. The purple contours in the two bottom frames indicate the region of maximum power coupling. Reprinted from ref. 128 with permission from Elsevier.

becomes too long for efficient ionization of the sample (see below).

The calculated gas flow path lines for this range of injector gas flow rates, as well as for two larger values, are plotted in Fig. 14. The other conditions are again kept the same. At low injector gas flow rates (~0.3–0.4 L min^{-1}) the injector gas is clearly subject to recirculation and no central channel is formed, as could also be deduced from previous figure. An injector gas flow rate between 0.6 and 0.8 L min^{-1} results in some slight deviation in the injector gas flow pattern, but above 1 L min^{-1}, it goes in a (more or less) straight line towards the sampler, which is required to optimize the sample transport to the MS. This observation is in good agreement with the measurements of Gamez *et al.*, who also reported that the central channel becomes well-defined only at flow rates above 1 L min^{-1}.[31]

Besides the injector gas, the auxiliary gas flow exhibits an even more pronounced recirculation behavior, at all injector gas flow rates below 1.6 L min^{-1}, as is obvious from Fig. 14. The effect becomes somewhat less pronounced at higher injector gas flow rates, but only around 1.8 L min^{-1}, the auxiliary gas seems to go straight towards the sampler. In the latter case, however, it does not pass through the region of high power coupling (*cf.* the purple contours in the two lowest panels of Fig. 14), hence this limits the heat transfer to the injector gas. This can explain why in experiments the transport efficiency of aerosols drops at flow rates above 1.4 L min^{-1}.[22] We can conclude, based on Fig. 13 and 14, that an injector gas flow rate of around 1–1.2 L min^{-1} seems to be optimal, for the conditions presented here. More details about this study can be found in ref. 128. It should, however, be mentioned that this conclusion does not yet involve the effect of the injector gas flow rate on the Cu sample behavior, as predicted by our model. Below we will show the Cu sample evaporation rate, ion density profiles and sample transport efficiency to the sampling cone, as a function of the injector gas flow rate, and it will be illustrated that the optimal flow rate is somewhat lower (around 0.8 L min^{-1}; see further), because a too high flow rate reduces the analyte atomization and ionization due to the lower temperature.

The minimum value of the injector gas flow rate to avoid recirculation of the auxiliary gas, *i.e.*, the so-called transition

point, seems to be strongly dependent on the auxiliary gas flow rate itself.[130] This is illustrated in Fig. 15: the transition point in the injector gas flow rate clearly rises upon rising value of the auxiliary gas flow rate. For instance, at an auxiliary gas flow rate of 0.4 L min^{-1}, the transition point to avoid recirculation of the auxiliary gas is reached at an injector gas flow rate of 1.8 L min^{-1} (*cf.* also Fig. 14 above), while at auxiliary gas flow rates of 0.6 L min^{-1}, 0.8 L min^{-1} and 1.0 L min^{-1}, the transition point in the injector gas flow rate rises to 2.0, 2.2 and 2.5 L min^{-1}, respectively. It should, however, be noted that the highest flow rates depicted here are at the limit of the present model, because the Reynold's number approaches here the limit of laminar flow. Nevertheless, the trend is clear. Note that a higher outer gas flow rate will also reduce the recirculation of the auxiliary gas, but the effect is less pronounced than for the effect of the injector gas flow rate.[130]

To demonstrate in more detail the correlation between injector gas and auxiliary gas flow rate, we plot in Fig. 16 the gas flow path lines for various combinations of both flow rates. Only the upper half of the ICP is shown, but the lower half is exactly the same, due to the cylindrical symmetry of the ICP. As is clear from this figure, when the injector gas flow rate is larger than the auxiliary gas flow rate, only the injector gas can pass through the sampler orifice, while in case that the injector gas flow rate is smaller than or equal to the auxiliary gas flow rate, also part of the auxiliary gas can pass through the sampler orifice. Again, as discussed in Section 4.4 above, the condition that is most favorable will depend on the sample ion cloud size. Indeed, if the sample ion cloud is small, so that it is only transported by the injector gas, the first situation will be desired, but when the sample ion cloud is larger, so that part of it is transported by the auxiliary gas, the second situation will be more beneficial.

It should be realized that this thumb rule is only valid as long as the auxiliary gas flow rate is not too high or too low. Indeed, for auxiliary gas flow rates of 0.3 L min^{-1}, some fraction of the auxiliary gas can still pass through the sampler orifice, even when the injector gas flow rate is slightly higher. On the other hand, for auxiliary gas flow rates in the order of 1.2 L min^{-1}, the auxiliary gas cannot pass through the sampler orifice, even when its flow rate is higher than the injector gas flow rate. A more detailed discussion about these results can be found in ref. 128.

Finally, as discussed in Section 4.5 above, the injector gas can also exhibit recirculation behavior, especially at larger injector inlet diameters. This was also studied in detail in ref. 130. Again, like for the auxiliary gas, the backward motion in the injector gas path lines can be avoided by applying higher injector gas flow rates. Furthermore, it can be reduced (but not completely avoided, at the conditions investigated) by applying a higher auxiliary gas flow rate. The outer gas flow rate, on the other hand, seems to have no effect on the recirculation behavior of the injector gas. More details about the effect of the injector gas, auxiliary gas and outer gas flow rates on the backward motion of the injector gas can be found in ref. 130.

Besides the effect on the gas flow path lines, we have also investigated the effect of the injector gas flow rate on the sample behavior. Our calculations reveal that the analyte evaporation and ionization will strongly be shifted downstream upon higher

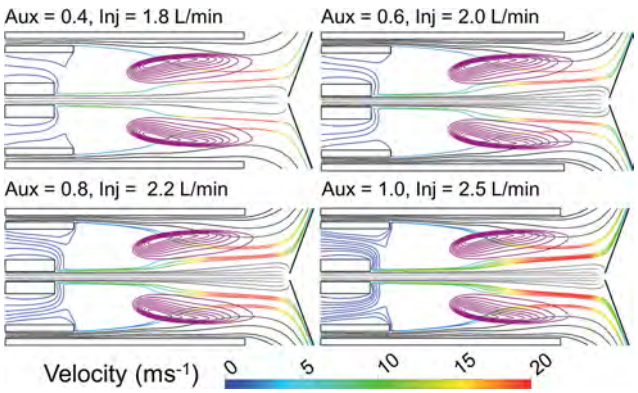

Fig. 15 2D gas flow velocity path lines originating from the auxiliary gas inlet, colored by velocity in m s^{-1}, as well as from the injector gas and outer gas inlets, colored in black, at different values of the injector gas and auxiliary gas flow rates, as indicated above the panels. For each auxiliary gas flow rate given (Aux), the corresponding injector gas flow rate (Inj) indicates the transition point, or minimum value needed to avoid (major) recirculation in the auxiliary gas. The other conditions are the same as in Fig. 5. The purple contours indicate the region of maximum power coupling.

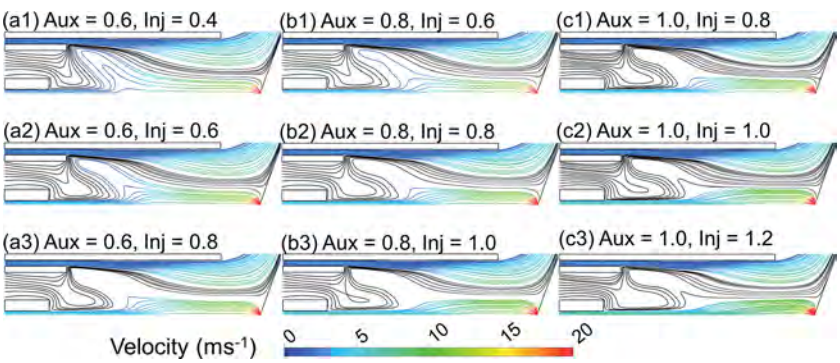

Fig. 16 2D gas flow velocity path lines originating from the injector gas and outer gas inlets, colored by velocity in m s^{-1}, and from the auxiliary gas inlet, colored in black, at (a) 0.6, (b) 0.8 and (c) 1.0 L min^{-1} of auxiliary gas flow rate. The injector gas flow rate is (1) lower than, (2) equal to and (3) higher than the auxiliary gas flow rate. Only half of the 2D axisymmetric torch is plotted. Reprinted from ref. 128 with permission from Elsevier.

injector gas flow rate. This is clearly illustrated in Fig. 17, showing the spatial range, in the axial direction, in which the evaporation takes place, for different injector gas flow rates. For the sake of clarity, the position of the coils and of the sampler are also indicated. At an injector gas flow rate of 0.4 L min^{-1}, the region of evaporation is quite limited in space, and it occurs near the first winding of the coil, while at the largest injector gas flow rates, it extends from midway the first and second winding of the coil till close to the sampler. This can be explained by the higher transport velocity of the injector gas in the ICP, but especially due to the lower temperature, resulting from the larger amount of cold gas volume injected. Indeed, the length of the cool central channel clearly rises with rising injector gas flow rate, as demonstrated in Fig. 13 above.

On the other hand, in spite of the larger region in which evaporation takes place, the total amount of Cu evaporation, integrated over the entire torch, drops more or less linearly upon increasing injector gas flow rate, as is shown in Fig. 18. Also the maximum evaporation rate drops nearly linearly with increasing injector gas flow rate, from above 0.8 ng s^{-1} at an injector gas flow rate of 0.4 L min^{-1}, to about 0.55 ng s^{-1} at the highest injector gas flow rates investigated. This drop in evaporation rate is of course again due to the lower temperature, as mentioned above.

Fig. 19 illustrates the Cu^+ ion density profiles for four different values of the injector gas flow rate, keeping the other conditions the same. The black contour lines indicate the temperature profiles, to explain the behavior in the Cu ionization. They are plotted in the same scale for the four cases, ranging from 0 K to 10 000 K. For the sake of clarity, the contour lines are labeled, and the meaning of the labels is indicated under the figures. Obviously, the highest temperature contour lines (indicating the area in the ICP above 9000 K and 10 000 K) become smaller and shift away from the central axis upon rising injector gas flow rate. At the 1.2 and 1.6 L min^{-1}, the temperature will even not reach 10 000 K anymore. Thus, a higher injector gas flow rate leads to a longer cool central channel inside the ICP, as also illustrated in Fig. 13 above.

Note that the same color scale is used for the ion density profiles in each case, to allow easy comparison, but the maximum values of the ion density are quite different, *i.e.*, 5.3×10^{18} m^{-3}, 3.5×10^{18} m^{-3}, 2.4×10^{18} m^{-3}, and 1.9×10^{18} m^{-3}, for the carrier gas flow rates of 0.4, 0.8, 1.2 and 1.6 L min^{-1}, respectively. Furthermore, not only the absolute values but also the ion cloud size changes significantly upon rising injector gas flow rate. At low injector gas flow rate, the ionization is clearly more pronounced, due to the higher plasma temperature, and for the same reason it occurs earlier in space, with the ion cloud expanding more in the radial direction, while at high flow rate, the ion cloud is smaller and closer to the central axis and the sampler. This reduction in ion cloud size upon rising injector gas flow rate was also observed from side-on fluorescence images in literature.[145] When the ion cloud size is large due to more radial diffusion, like in Fig. 19(a), we can thus shift it towards the sampler by applying a higher injector gas flow rate, as illustrated in Fig. 19(b–d). However, at the same time, the amount of ionization drops, leading to clearly lower ion densities, because of the lower plasma temperature.

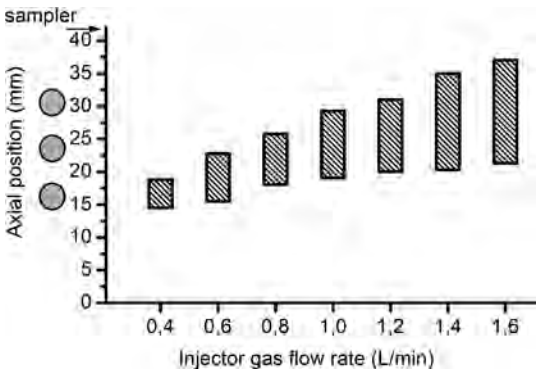

Fig. 17 Spatial range of evaporation in the axial direction, as a function of injector gas flow rate. The other conditions are specified in Fig. 5 and 6.

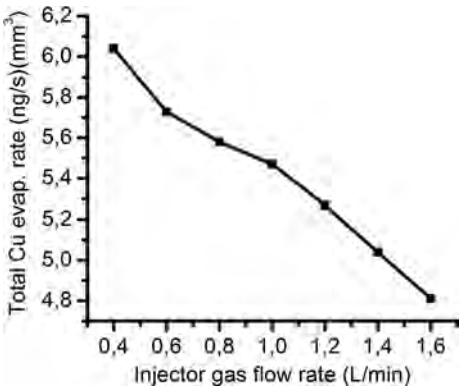

Fig. 18 Total Cu sample evaporation rate, integrated over the entire torch, as a function of the injector gas flow rate. The other conditions are specified in Fig. 5 and 6.

The downstream shift in analyte vaporization and ionization upon increasing the injector gas flow rate is in agreement with experimental observations[43,58,59,145] and computer modeling[88] from literature. We should note that, compared to aerosol droplet introduction, the elemental particles considered here, originating *e.g.* from LA, will start to evaporate earlier when they penetrate into the ICP, as no desolvation step needs to be taken first. Thus, the analyte diffusion will begin further upstream in the ICP and the ion cloud will be larger at the position of the sampler than with aerosol particles, thus decreasing the analyte ion detection efficiency. In order to increase the ion detection efficiency of LA-ICP-MS, the region of high plasma temperature should be shifted downstream, *e.g.*, by increasing the injector gas flow rate, as also reported by Niemax and colleagues.[58]

Finally, in Fig. 20 we plot the fractions of Cu^+ ions and Cu^0 atoms at the sampler and of Cu^0 atoms leaving the ICP through the open ends, with respect to the total amount of Cu at the inlet, as a function of the injector gas flow rate. The fraction of Cu^{2+} ions is again not shown, because it is negligible. The fraction of Cu^0 atoms passing through the sampler orifice is around 8.5% at low injector gas flow rate, and it rises up to about 28% at the highest injector gas flow rate, while the

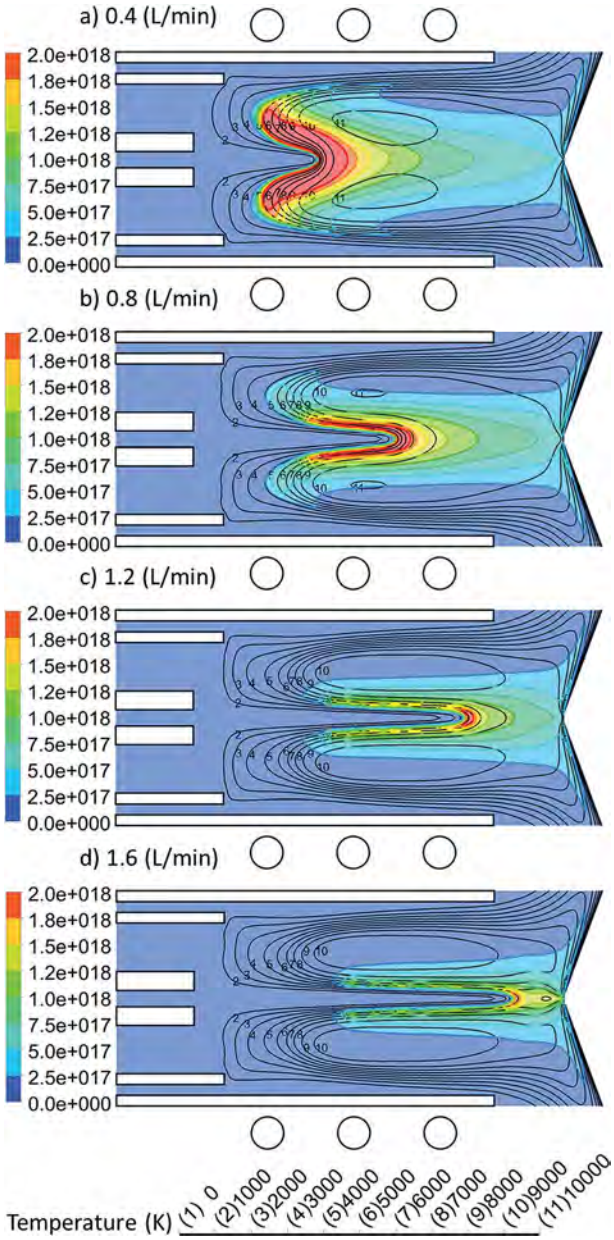

Fig. 19 2D Cu^+ ion number density profiles at four different injector gas flow rates, *i.e.*, 0.4 (a), 0.8 (b), 1.2 (c) and 1.6 (d) L min^{-1}, as well as the plasma temperature profiles (black contours) ranging from 0 to 10 000 K (see explanation of the labels at the bottom of the figure). The other conditions are specified in Fig. 5 and 6.

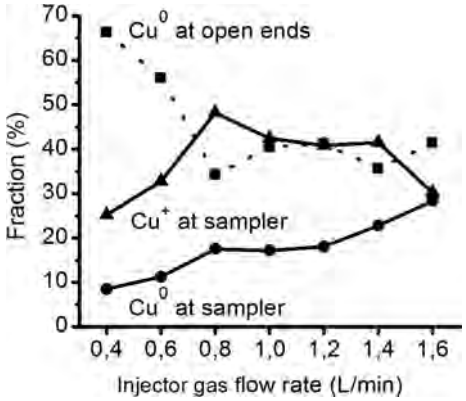

Fig. 20 Fraction of Cu^+ and Cu^0 at the sampler and fraction of Cu^0 leaving at the open ends, with respect to the total amount of Cu at the inlet, as a function of the injector gas flow rate. The other conditions are specified in Fig. 5 and 6.

fraction of Cu^0 atoms leaving the ICP through the open ends drops from *ca.* 66% at 0.4 L min^{-1} to 34–41% at injector gas flow rates between 0.8 and 1.6 L min^{-1}. However, as mentioned above, the most important is the fraction of Cu^+ ions passing through the sampler orifice, because it is a measure for the sample transport efficiency from the injector gas inlet till entering the MS interface. At low injector gas flow rates, this fraction rises with the flow rate, from 25% at 0.4 L min^{-1}, to 48% at 0.8 L min^{-1}, followed by a drop to 30% at the highest injector gas flow rate of 1.6 L min^{-1}. This can be explained from the Cu^+ ion density profiles plotted in previous figure. Indeed, at low injector gas flow rates, rising the flow rate leads to a downstream shift of the ion cloud, explaining the rise in Cu^+ fraction at the sampler, but at too high flow rates, the analyte atomization and ionization is limited due to the lower temperature, explaining why further increasing the injector gas flow rate above 0.8 L min^{-1} does not increase the fraction of Cu^+ ions at the sampler.

4.7. Effect of the plasma power

The effect of applied power on the plasma temperature is presented in Fig. 21, keeping the injector gas, auxiliary gas and outer gas flow rates fixed at 1 L min^{-1}, 0.4 L min^{-1} and 12 L min^{-1}, respectively. Increasing the applied power results in a higher plasma temperature, as expected. This will also enhance the ionization in the coil region, and thus the electron density. On the other hand, a higher power also reduces the length of the cool central channel (see small black lines above each panel in Fig. 21), which has consequences for the sample evaporation and ionization, as will be discussed below.

Furthermore, the applied power affects the gas flow path lines, as is clear from Fig. 22. Indeed, at higher applied power, the backward motion of the auxiliary gas is obviously reduced. This was also confirmed experimentally. Indeed, experiments were performed on an Elan 6000 ICP-MS (Perkin Elmer), by introducing NaCl aerosols generated by LA into the ICP from the auxiliary gas inlet, and recording the Na atomic emission line at 589 nm with an ICCD camera.[130] At low power, a curved gas flow pattern, indicative for rotational motion, was observed, while there was no evidence for the latter at high power. More details about these experiments can be found in ref. 130.

As a consequence of this reduced rotational motion at higher power, Fig. 22 illustrates that at 1500 W, the auxiliary gas cannot pass through the region of maximum power coupling anymore, causing less efficient heating in the plasma. At the same time, however, the outer gas now passes through the region of maximum power coupling, thereby reducing the cooling efficiency. We showed in our recent paper that a further increase in applied power does not have any added value.[133]

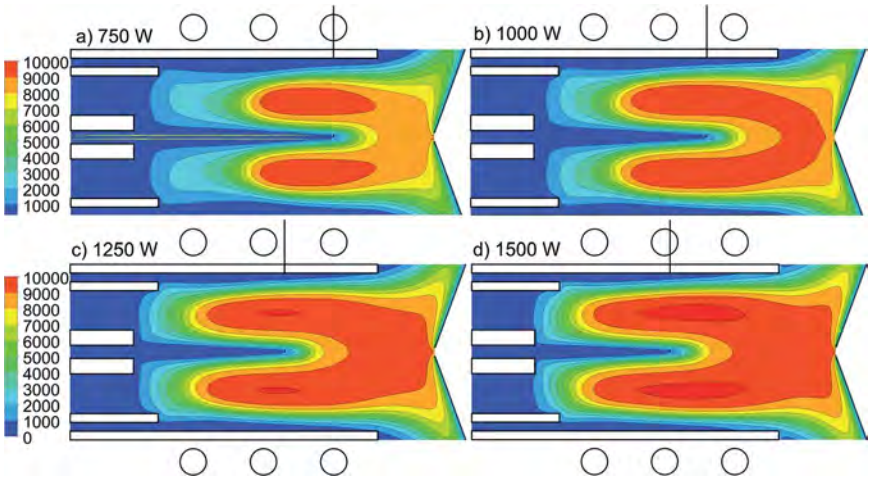

Fig. 21 2D plasma temperature profiles, at an applied power of 750 W (a), 1000 W (b), 1250 W (c) and 1500 W (d). The other conditions are the same as in Fig. 5. The small black lines above each panel indicate the length of the cool central channel.

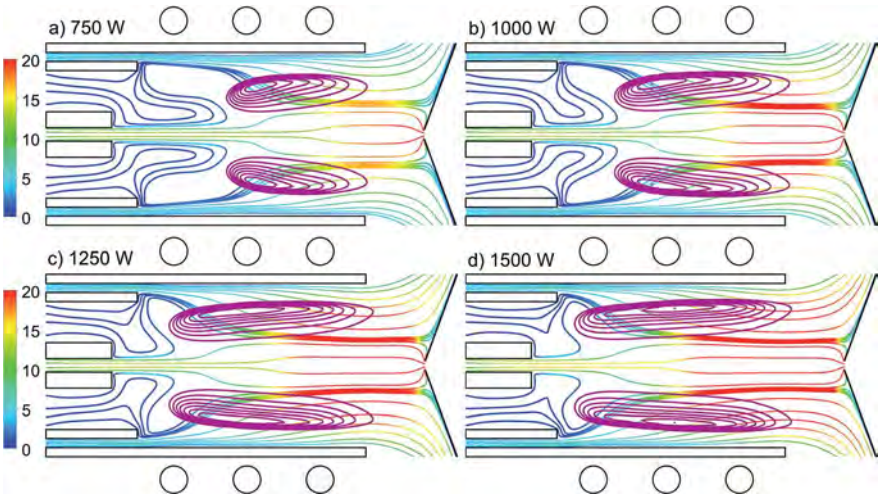

Fig. 22 2D gas flow velocity path lines of the injector gas, auxiliary gas and outer gas, colored by velocity in m s^{-1}, at an applied power of 750 W (a), 1000 W (b), 1250 W (c) and 1500 W (d). The other conditions are the same as in Fig. 5. The purple contours indicate the region of maximum power coupling.

As illustrated in Fig. 21 above, a higher applied power leads to a drop in the length of the cool central channel. Consequently, the sample evaporation will take place somewhat earlier in the torch, as is clear from Fig. 23. This was also reported in literature, both from experimental studies[145–147] and computer simulations.[87,88,148]

In ref. 133 we plotted the 2D Cu^+ ion density profiles for different values of applied power, and we showed that the shift in sample evaporation to earlier positions in the ICP upon increasing power causes also the ionization to take place earlier in space. Moreover, the Cu^+ ion density profiles become more concentrated near the central axis with rising power,[133] which was also reported from fluorescence images in literature,[143] and in addition, a second maximum arises near the sampler, attributed to ionization of the Cu particles injected on-axis. Indeed, the latter are able to travel in a straight line along the central axis, leading to evaporation and ionization on the axis and more downstream in the plasma as discussed in Section 4.5 above.

In Fig. 24, the effect of the applied power on the calculated fractions of Cu^0 atoms and Cu^+ ions entering the MS sampling cone is depicted, as well as on the fraction of Cu^0 atoms leaving

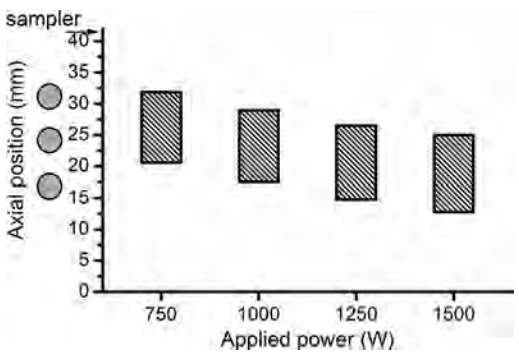

Fig. 23 Spatial range of evaporation in the axial direction, as a function of applied power. The other conditions are specified in Fig. 5 and 6.

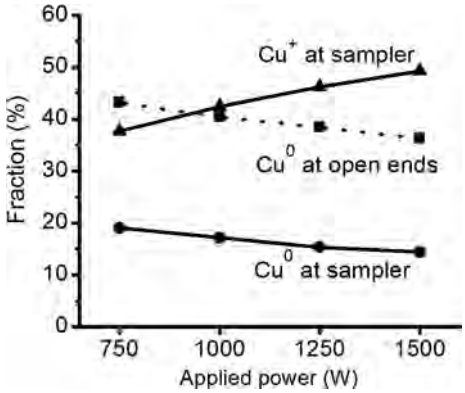

Fig. 24 Fraction of Cu^+ and Cu^0 at the sampler and fraction of Cu^0 leaving at the open ends of the ICP, with respect to the total amount of Cu at the inlet, as a function of the applied power. The other conditions are specified in Fig. 5 and 6.

the ICP through the open ends. The other conditions are the same as before. The fraction of Cu^{2+} ions is again negligible, and therefore not shown. The fraction of Cu^0 atoms leaving the ICP through the open ends is around 35–45%, slightly decreasing with power, while the fraction of Cu^0 passing through the sampler orifice decreases slightly from 20% to 15% with rising applied power. As mentioned above, the most important is however the fraction of the injected Cu sample that will pass through the MS interface as Cu^+ ions. This fraction is around 38–50%, slightly increasing with increasing power. This is attributed to the higher plasma temperature, giving rise to more ionization. The effect is, however, not so pronounced, given the opposite effect of the somewhat earlier evaporation at higher power (*cf.* Fig. 23 above). Our model predictions indicate that further increasing the power will not result in a further increase of the fraction of Cu^+ ions entering the MS interface, as shown in our recent paper.[133]

4.8. Effect of particle diameter

Fig. 25 illustrates the 2D trajectories of Cu particles with various diameters (ranging between 10 nm and 100 μm), which are injected at a flow rate of 100 ng s^{-1} from the whole 1.5 mm width of the injector gas inlet, colored according to their temperature, along with the Ar gas flow path lines, colored in black. The other conditions are the same as in Fig. 5 and 6.

It is clear that the smaller particles (especially up to 1 μm diameter) are evaporated earlier in the torch than the larger particles, which obviously need more time and a higher temperature to become evaporated. The particles with 100 μm diameter seem not to evaporate to a large extent at the conditions under study, and mostly stay in the liquid phase even when reaching the sampler. If they would pass through the sampler orifice in liquid phase, they would lower the detection efficiency of the ICP.[57,61] Moreover, those particles that move in the radial direction will hit the cooled sampler cone and get stuck there, which results also in sample loss. Thus, it seems that at the conditions under study, these large particles cannot be efficiently sampled.

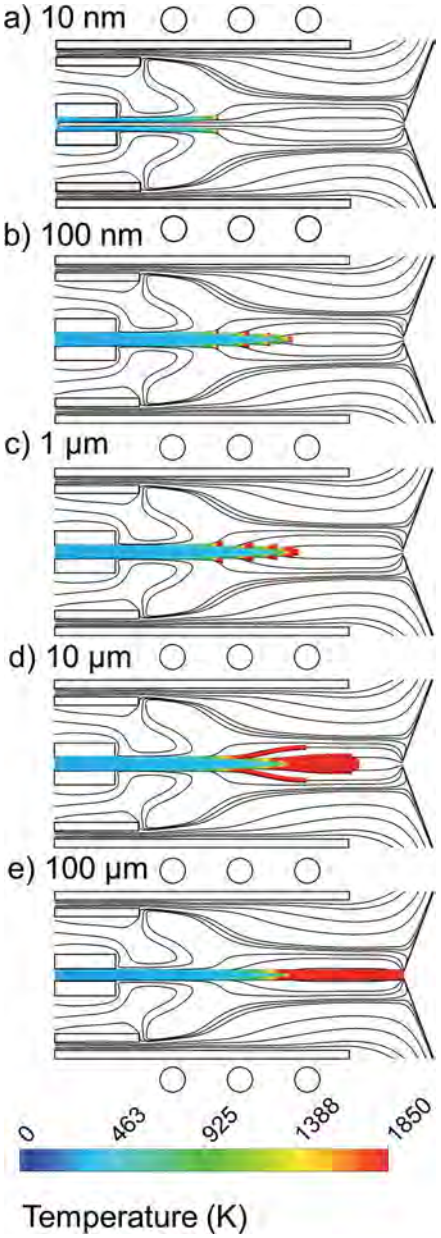

Fig. 25 Effect of particle diameter on the 2D trajectories of Cu particles, colored according to their temperature, as well as the Ar gas flow path lines originating from injector gas, auxiliary gas and outer gas, colored in black. The other conditions are specified in Fig. 5 and 6.

These findings correlate well with experimental results from literature. Niemax and colleagues also reported that larger particles penetrate deeper into the ICP than smaller particles, before they are desolvated.[57,58] Likewise, Olesik and Hobbs found that droplets of 16 μm diameter and above can survive for 8 mm above the load coil, while droplets of 31 μm diameter and above can survive for 18 mm above the load coil.[43] Finally, Hieftje and colleagues, in the case of flame spectrometry, observed a linear relationship between the square of the droplet diameter and the time of desolvation, which can be correlated with the penetration depth into the plasma.[149,150]

The 2D Cu^+ ion density profiles for these different Cu particle diameters are plotted in Fig. 26. Note that the color scale is the same in each case (except for panel (e)), to allow easy comparison. The Cu^+ ion density clearly rises upon increasing particle diameter, up to 10 μm, after which it strongly drops again for the larger particles of 100 μm diameter (note that the color scale for panel (e) indicates 10× lower values, as otherwise no density profile would be visible). The reason for the initial rise is that the smallest particles evaporate earlier in the torch, where the plasma temperature is still lower, and thus the ionization is less efficient. On the other hand, the largest particles almost do not evaporate, so as a consequence, the corresponding Cu^+ ion density is very low. Hence, this explains why the Cu^+ ion density reaches a maximum at a particle diameter of 10 μm.

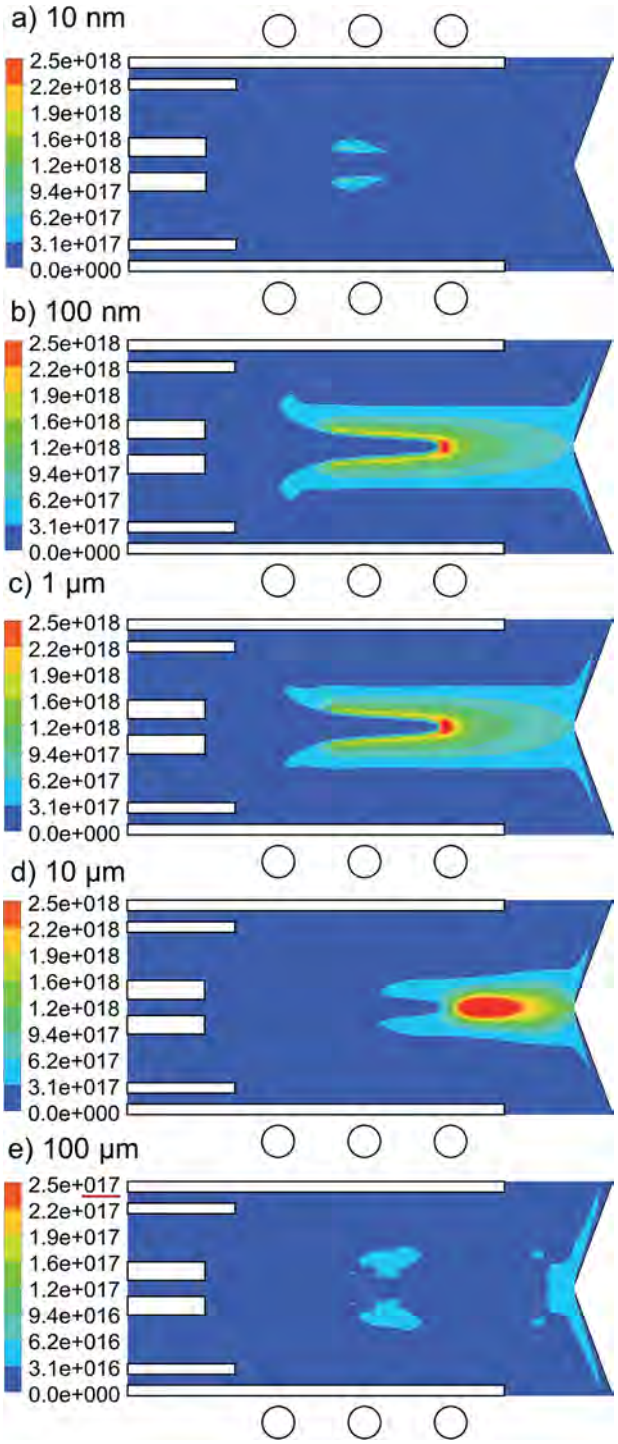

Fig. 26 2D Cu^+ ion number density profiles for different Cu particle diameters. The other conditions are specified in Fig. 5 and 6. Note that the color scale for panel (e) indicates 10× lower values, as otherwise no density profile would be visible here.

Furthermore, it is clear from Fig. 26 that for the larger particles (up to 10 μm diameter), the maximum Cu^+ ion density shifts closer to the sampler, again because they evaporate later in space, which is beneficial for sample transport to the MS. The latter can indeed be deduced from Fig. 27. The fraction of Cu^+ ions passing through the sampler orifice with respect to the amount of Cu injected into the ICP, or in other words the Cu sample transport efficiency towards the MS interface, slightly rises from 38% to 50% when the particle diameter rises from 10 nm to 10 μm, but it significantly drops for the particles of 100 μm diameter, because they are not efficiently evaporated. The fraction of Cu^0 passing through the open ends follows the opposite trend, with values between 30 and 60%, while the fraction of Cu^0 passing through the sampler remains more or

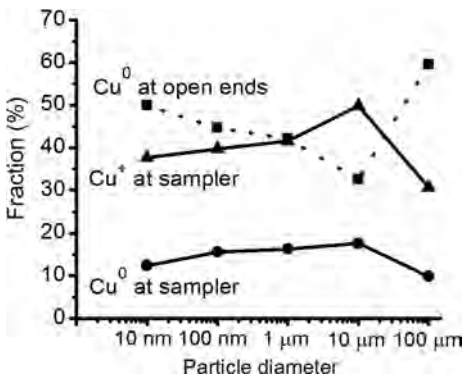

Fig. 27 Fraction of Cu^+ and Cu^0 at the sampler and fraction of Cu^0 leaving at the open ends of the ICP, with respect to the total amount of Cu at the inlet, as a function of the particle diameter. The other conditions are specified in Fig. 5 and 6.

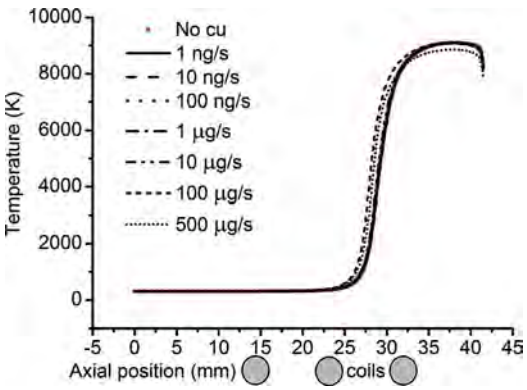

Fig. 28 Plasma temperature along the central channel, for different Cu mass loading flow rates, as indicated in the legend. The other conditions are specified in Fig. 5 and 6.

less constant at 10–15%. Hence, at the conditions investigated here, Cu particles up to 10 μm diameter can be efficiently evaporated, ionized and transferred as Cu^+ ions towards the MS interface, but for larger particles, the present conditions are not beneficial, and we expect that a higher power (yielding a higher temperature) or a lower injector gas flow rate would be needed.

4.9. Effect of particle mass loading flow rate

To investigate the effect of the particle mass loading flow rate, we carried out calculations for Cu particle flow rates between 1 ng s^{-1} and 500 μg s^{-1}.[132] Fig. 28 illustrates the calculated temperature along the central channel for the different mass loading flow rates investigated, as well as the case without Cu injection. It is clear that a particle loading flow rate up to 10 μg s^{-1}, and even 100 μg s^{-1}, has only minor effect on the plasma temperature. Some cooling effect is observed at a mass loading flow rate of 500 μg s^{-1}, so it would take a bit longer before the injected material is sufficiently heated to become fully evaporated, and also the ionization of the sample material would be slightly affected. However, even at 500 μg s^{-1}, the effect on the temperature is minor. It should be mentioned that the range of particle loading flow rates investigated here is applicable to LA-ICP-MS, where elemental particles are introduced, and a mass loading flow rate of 500 μg s^{-1} is far above the values typically used,[140] so that we can safely conclude that for typical mass loading flow rates used in LA-ICP-MS, the sample loading will not affect the plasma temperature.

It should be mentioned that for aqueous analyte solutions, feed rates up to 0.1 g min^{-1} (or 1.7 mg s^{-1}) can be used, and even for these flow rates, it was reported that the plasma temperature is not affected by the sample introduction.[56–58] However, in our model, we inject pure Cu particles and not samples diluted in water. In the latter case, the situation is more complicated, because when the sample is introduced in the ICP, the plasma is affected by desolvation, dissociation of the water molecules, and by excitation and ionization of these dissociation products, and only a minor fraction of real sample is subject to excitation and ionization, while in our case, the particles consist of pure Cu, that will all need to be evaporated, excited and/or ionized. Therefore, we expect that for similar mass loading flow rates, the local cooling effect of the plasma will indeed be less significant when the analyte is diluted in water.

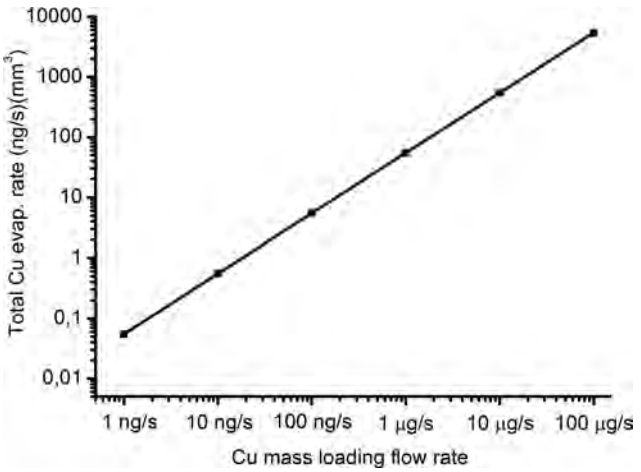

Fig. 29 Total Cu sample evaporation rate, integrated over the entire torch, as a function of the Cu particle mass loading flow rate. The other conditions are specified in Fig. 5 and 6.

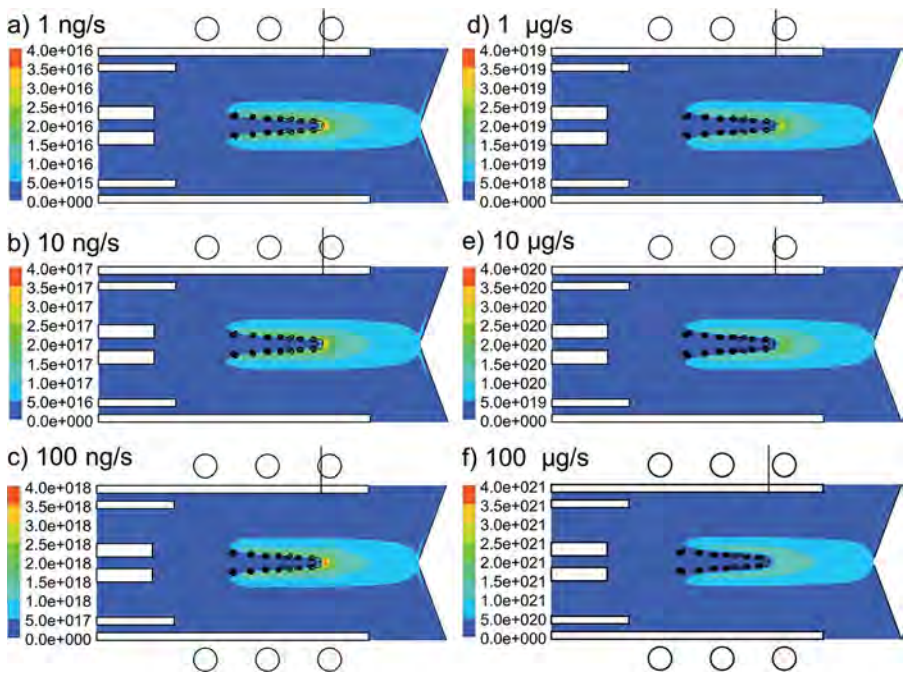

Fig. 30 2D Cu^+ ion number density profiles, as well as the contours of the Cu evaporation rate, for 6 different Cu particle mass loading flow rates. The other conditions are specified in Fig. 5 and 6. The maximum position of evaporation is indicated with the thin black line above each panel.

In Fig. 29 we plot the total Cu evaporation rate, integrated over the entire torch, as a function of the Cu particle loading flow rate. The total evaporation rate obviously rises linearly upon increasing Cu particle loading flow rate, for all loading flow rates investigated, indicating that the evaporation efficiency is not affected by the mass loading flow rate. This is as expected, because the plasma temperature is not significantly affected.

The corresponding Cu^+ ion density profiles for Cu particle loading flow rates up to 100 μg s^{-1} are illustrated in Fig. 30. Note that the color scales are different in each panel, to clearly show where the maximum is reached in each case. The profiles have the same shape, but the maximum ion density rises somewhat less than linearly with the Cu mass loading flow rate. Hence, the ionization efficiency seems to slightly drop with increasing mass loading flow rate. The contours of the Cu evaporation rate are also indicated in the figure. Although the total evaporation rises linearly with the particle mass loading flow rate, as observed in Fig. 29, the position of evaporation slightly shifts to earlier positions in the torch upon higher mass loading flow rates. This is most apparent for the flow rate of 100 μg s^{-1}. This minor change still affects the Cu ionization efficiency, as the temperature gradients inside the torch are quite significant (see Fig. 28 above).

Finally, we plot in Fig. 31 the Cu^+ and Cu^0 fractions at the sampler orifice, as well as the Cu^0 fraction leaving the ICP at the open ends, with respect to the amount of Cu injected in the ICP, as a function of the Cu mass loading flow rate. It is clear that the fraction of Cu^0 leaving the ICP at the open ends stays more or less constant at a value around 35–40%. The fraction of Cu^0 entering the sampler rises with Cu mass loading flow rate, while the fraction of Cu^+ at the sampler clearly drops from 48% at the lowest loading flow rates, till about 17% at a particle loading flow rate of 100 μg s^{-1}. Hence, the small shift in evaporation towards earlier positions in the torch upon increasing mass loading flow rate, affect the ionization efficiency, as was apparent from Fig. 30, and the latter has clear consequences for the Cu sample transport efficiency, from injection into the ICP towards the MS interface.

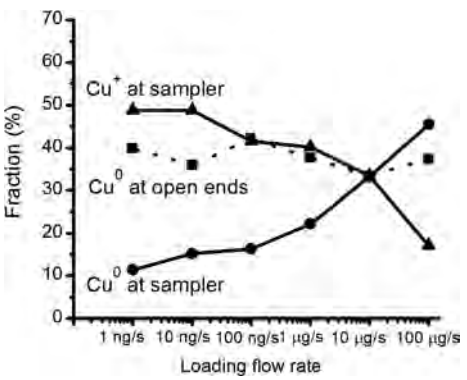

Fig. 31 Fraction of Cu^+ and Cu^0 at the sampler and fraction of Cu^0 leaving at the open ends of the ICP, with respect to the total amount of Cu at the inlet, as a function of the Cu particle mass loading flow rate. The other conditions are specified in Fig. 5 and 6.

5. Conclusions and outline for future developments

In this tutorial review paper, we presented our model, developed for an ICP torch connected to a MS interface, to obtain a better understanding of the underlying plasma processes of ICP-MS. We showed typical plasma characteristics, such as the plasma temperature and electron density profiles and the gas flow patterns throughout the ICP, as well as detailed information on the sample behavior, including Cu particle transport, evaporation and ionization, as well as the ion cloud distributions in the ICP and the fraction of Cu^+ ions passing the sampling cone, with respect to the amount of Cu injected into the ICP. The effect of various geometrical parameters, such as the sampling cone position and orifice diameter, and the injector gas inlet diameter, was presented, as well as the effect of the gas flow rates and applied power and of the sample characteristics, *i.e.*, particle diameter, mass loading flow rate and injection position. This information provides us insight into how the operating conditions and geometry can be optimized to improve the analytical performance of ICP-MS.

The present model only allows to treat elemental particles, as produced from *e.g.* LA. In this paper, we focus on Cu as sample material, but we are currently working on a comparison between Cu and Zn, to investigate whether different materials behave differently in the plasma, in terms of particle transport, evaporation and ionization, and how this affects the analytical signals. This is particularly relevant for the problem of fractionation, occurring in (LA-)ICP-MS for *e.g.* brass samples. In the future, we would like to extend this study also to other materials.

Furthermore, we would also like to investigate the effect of He addition to the Ar gas, which is also of special interest for LA-ICP-MS, because He is typically used as the carrier gas. In previous work, we already investigated the effect of He addition to the Ar plasma.[125] Although the model used for that study did not yet account for the sample behavior, it gave useful insights into the strong effects exerted by He addition to the Ar ICP. Indeed, the calculations revealed that the central channel became significantly longer and the plasma temperature was clearly higher than in case of using pure Ar. As a consequence, higher gas flow rates can be applied by the addition of He, and thus the gas velocity in the transport system towards the ICP can be increased, which allows shorter washout-times. The latter will enable shorter measurement times, which is of interest, *e.g.*, for spatial mapping analyses in LA-ICP-MS. Moreover, we expect that the higher plasma temperature and the longer effective plasma length will allow the injection of larger droplets into the ICP that can still become completely evaporated at the detection site. Thus, we expect that He addition will enhance the analytical performance of the ICP. More details can be found in ref. 125. As this earlier model did not yet include the sample behavior, we will investigate the effects of He addition in more detail with our new, complete model.

As a next step in our model development, we would like to describe the behavior of analyte material introduced into the ICP as aerosols (*e.g.*, multicomponent droplets diluted in

water). This is far more complicated, as the sample will also be subject to desolvation, besides the processes of heating, evaporation and ionization. Moreover, chemical reactions will take place between the dissolved elements and species originating from the water (like O, OH, H, …), which also will need to be described in the model.

Another possible improvement to our current model would be to extend it to 3D. Indeed, our model is now based on a 2D axisymmetric geometry, assuming that the coils are perpendicular to the ICP torch, while in reality the coils are wrapped around the torch, so they are not exactly perpendicular. Therefore, extending our model to 3D, to account for this effect, will further enhance the accuracy of our modeling work.

Finally, our current model describes the injected sample material transport, including ionization, up to the sampling cone, but the ion transport inside the MS is not yet accounted for in our current model. Spencer, Farnsworth and colleagues described the neutral Ar gas flow through the first vacuum stage of the ICP-MS by a Direct Simulation Monte Carlo model.[123,124] It would be interesting to extend the latter description, or a variation to it, to describe also the ion transport, and to combine this modeling approach with our model for the ICP. This would be the ultimate goal, to arrive at a complete description of ICP-MS.

Acknowledgements

The authors are very grateful to H. Lindner for the initial model development and for the many interesting discussions. They also gratefully acknowledge financial support from the Fonds voor Wetenschappelijk Onderzoek (FWO; Grant number 6713). The calculations were carried out using the Turing HPC infrastructure at the CalcUA core facility of the Universiteit Antwerpen (UAntwerpen), a division of the Flemish Supercomputer Center VSC, funded by the Hercules Foundation, the Flemish Government (department EWI) and the UAntwerpen.

References

1 A. Montaser, *Inductively coupled plasma mass spectrometry*, Wiley, New York, 1992.
2 A. Montaser, *Inductively coupled plasma mass spectrometry*, Wiley, New York, 1998.
3 R. S. Houk, V. A. Fassel, G. D. Flesch, H. J. Svec, A. L. Gray and C. E. Taylor, Inductively coupled argon plasma as an ion source for mass spectrometric determination of trace elements, *Anal. Chem.*, 1980, **52**, 2283–2289.
4 R. S. Houk, V. A. Fassel and H. J. Svec, Inductively coupled plasma-mass spectrometry: sample introduction, ionization, ion extraction, and analytical results in dynamic mass spectrometry, in *Dynamic Mass Spectrometry*, ed. D. Price and J. F. J. Todd, Heyden, London, 1981, vol. 6, ch. 19, pp. 234–251.
5 B. S. Duersch and P. B. Farnsworth, Characterization of the ion beam inside the skimmer cone of an inductively coupled plasma mass spectrometer by laser excited atomic and ionic fluorescence, *Spectrochim. Acta, Part B*, 1999, **54**, 545–555.
6 D. M. Chambers and G. M. Hieftje, Fundamental studies of the sampling process in an inductively coupled plasma mass spectrometer. II. Ion kinetic energy measurements, *Spectrochim. Acta, Part B*, 1991, **46**, 761–784.
7 A. L. Gray, R. S. Houk and J. G. Williams, Langmuir probe potential measurements in the plasma and their correlation with mass spectral characteristics in inductively coupled plasma mass spectrometry, *J. Anal. At. Spectrom.*, 1987, **2**, 13–20.
8 R. S. Houk, J. K. Schoer and J. S. Crain, Plasma potential measurements for inductively coupled plasma mass spectrometry with a center-tapped load coil, *J. Anal. At. Spectrom.*, 1987, **2**, 283–286.
9 I. I. Stewart, C. E. Hensman and J. W. Olesik, Influence of gas sampling on analyte transport within the ICP and ion sampling for ICP-MS studied using individual, isolated sample droplets, *Appl. Spectrosc.*, 2000, **54**, 164–174.
10 G. Meyer, R. Foster, A. Van der Hoeff, T. Albert, S. Luan, K. Hu, S. Karpova-Nadel and J. Schmeizel, Increasing laboratory productivity by combining ICP optical emission with ICP mass spectrometry, *Am. Lab.*, 1996, **28**, 21–24.
11 H. P. Longerich, Mass spectrometric determination of the temperature of an argon inductively coupled plasma from the formation of the singly charged monoxide rare earths and their known dissociation energies, *J. Anal. At. Spectrom.*, 1989, **4**, 491–497.
12 K. Lepla, M. A. Vaughan and G. Horlick, Simultaneous atomic emission and mass spectrometric measurements on an inductively coupled plasma, *Spectrochim. Acta, Part B*, 1991, **46**, 967–973.
13 R. S. Houk and Y. Zhai, Comparison of mass spectrometric and optical measurements of temperature and electron density in the inductively coupled plasma during mass spectrometric sampling, *Spectrochim. Acta, Part B*, 2001, **56**, 1055–1067.
14 R. S. Houk, J. K. Schoer and J. S. Crain, Deduction of excitation temperatures for various analyte species in inductively coupled plasmas from vertically-resolved emission profiles, *Spectrochim. Acta, Part B*, 1987, **42**, 841–852.
15 L. Pei-Qi, G. Pei-Zhing, L. Tei-Zheng and R. S. Houk, Langmuir probe measurements of electron temperature in an ICP, *Spectrochim. Acta, Part B*, 1988, **43**, 273–285.
16 H. Niu and R. S. Houk, Fundamental aspects of ion extraction in inductively coupled plasma mass spectrometry, *Spectrochim. Acta, Part B*, 1996, **51**, 779–815.
17 J. S. Crain, F. G. Smith and R. S. Houk, Mass spectrometric measurement of ionization temperature in an inductively coupled plasma, *Spectrochim. Acta, Part B*, 1990, **45**, 249–259.
18 R. S. Houk, B. R. LaFreniere, H. B. Lim and V. A. Fassel, Extraction discharge source for enhancing analyte line intensities in inductively coupled plasma atomic emission spectrometry, *Appl. Spectrosc.*, 1987, **41**, 391–395.
19 R. K. Winge, J. S. Crain and R. S. Houk, A high speed photographic study of plasma fluctuations and undissociated particles in ICP-MS, *J. Anal. At. Spectrom.*, 1991, **6**, 601–604.

20 H. Ma, N. Taylor and P. B. Farnsworth, The effect of the sampling interface onspatial distributions of barium ions and atoms in an inductively coupled plasma ion source, *Spectrochim. Acta, Part B*, 2009, **64**, 384–391.
21 S. A. Lehn, K. A. Warner, M. Huang and G. M. Hieftje, Effect of an inductively coupled plasma mass spectrometry sampler interface on electron temperature, electron number density, gas-kinetic temperature and analyte emission intensity upstream in the plasma, *Spectrochim. Acta, Part B*, 2002, **57**, 1739–1751.
22 J. H. Macedone, D. J. Gammon and P. B. Farnsworth, Factors affecting analyte transport through the sampling orifice of an inductively coupled plasma mass spectrometer, *Spectrochim. Acta, Part B*, 2001, **56**, 1687–1695.
23 B. S. Duersch, Y. Chen, A. Ciocan and P. B. Farnsworth, Optical measurements of ion density in the second vacuum stage of an inductively coupled plasma mass spectrometer, *Spectrochim. Acta, Part B*, 1998, **53**, 569–579.
24 S. Kaneco, T. Nomizo, T. Tanaka, N. Mizutani and H. Kawaguchi, Optimization of operating conditions in individual airborne particle analysis by inductively coupled plasma mass spectrometry, *Anal. Sci.*, 1995, **11**, 835–840.
25 W. G. Diegor and H. P. Longerich, Parameter interaction in signal optimization of an ICP mass spectrometer, *At. Spectrosc.*, 2000, **21**, 111–117.
26 H. P. Longerich, B. J. Fryer, D. F. Strong and C. J. Kantipuly, Effects of operating conditions on the determination of the rare earth elements by inductively coupled plasma-mass spectrometry (ICP-MS), *Spectrochim. Acta, Part B*, 1987, **42**, 75–92.
27 S. E. Long and R. M. Brown, Optimization in inductively coupled plasma mass spectrometry, *Analyst*, 1986, **111**, 901–906.
28 Q. Xie and R. Kerrich, Optimization of operating conditions for improved precision of zirconium and hafnium isotope ratio measurement by inductively coupled plasma mass spectrometry (ICP-MS), *J. Anal. At. Spectrom.*, 1995, **10**, 99–103.
29 B. T. G. Ting and M. Janghorbani, Optimization of instrumental parameters for the precise measurement of isotope ratios with inductively coupled plasma mass spectrometry, *J. Anal. At. Spectrom.*, 1988, **3**, 325–336.
30 G. Gamez, S. A. Lehn, M. Huang and G. M. Hieftje, Effect of mass spectrometric sampling interface on the fundamental parameters of an inductively coupled plasma as a function of its operating conditions. Part I. Applied RF power and vacuum, *Spectrochim. Acta, Part B*, 2007, **62**, 357–369.
31 G. Gamez, S. A. Lehn, M. Huang and G. M. Hieftje, Effect of mass spectrometric sampling interface on the fundamental parameters of an inductively coupled plasma as a function of its operating conditions. Part II. Central-gas flow rate and sampling depth, *Spectrochim. Acta, Part B*, 2007, **62**, 370–377.
32 J. H. Macedone, A. A. Mills and P. B. Farnsworth, Optical measurements of ion trajectories through the vacuum interface of an inductively coupled plasma mass spectrometer, *Appl. Spectrosc.*, 2004, **58**, 463–467.
33 A. L. Gray and A. R. Date, Inductively coupled plasma source mass spectrometry using continuum flow ion extraction, *Analyst*, 1983, **108**, 1033–1050.
34 G. M. Hieftje and G. H. Vickers, Developments in plasma source/mass spectrometry, *Anal. Chim. Acta*, 1989, **216**, 1–24.
35 F. E. Lichte, A. L. Meier and J. G. Crock, Determination of the rare-earth elements in geological materials by inductively coupled plasma mass spectrometry, *Anal. Chem.*, 1987, **59**, 1150–1157.
36 J. S. Crain, R. S. Houk and F. G. Smith, Matrix interferences in inductively coupled plasma-mass spectrometry: some effects of skimmer orifice diameter and ion lens voltages, *Spectrochim. Acta, Part B*, 1988, **43**, 1355–1364.
37 M. A. Vaughan and G. Horlick, Effect of sampler and skimmer orifice size on analyte and analyte oxide signals in inductively coupled plasma mass spectrometry, *Spectrochim. Acta, Part B*, 1990, **45**, 1289–1299.
38 H. P. Longerich, B. J. Fryer, D. F. Strong and C. J. Kanttpuly, Effects of operating conditions on the determination of the rare earth elements by inductively coupled plasma-mass spectrometry (ICP-MS), *Spectrochim. Acta, Part B*, 1987, **42**, 75–92.
39 D. Günther, H. P. Longerich, S. E. Jackson and L. Forsythe, Effect of sampler orifice diameter on dry plasma inductively coupled plasma mass spectrometry (ICP-MS) backgrounds, sensitivities, and limits of detection using laser ablation sample introduction, *Fresenius' J. Anal. Chem.*, 1996, **355**, 771–773.
40 N. Taylor and P. B. Farnsworth, Experimental characterization of the effect of skimmer cone design on shock formation and ion transmission efficiency in the vacuum interface of an inductively coupled plasma mass spectrometer, *Spectrochim. Acta, Part B*, 2012, **69**, 2–8.
41 R. K. Winge, J. S. Crain and R. S. Houk, A high speed photographic study of plasma fluctuations and undissociated particles in ICP-MS, *J. Anal. At. Spectrom.*, 1991, **6**, 601–604.
42 J. W. Olesik, Investigating the fate of individual sample droplets in inductively coupled plasmas, *Appl. Spectrosc.*, 1997, **51**, 158A–175A.
43 J. W. Olesik and S. E. Hobbs, Monodisperse dried microparticulate injector: a new tool for studying fundamental processes in inductively coupled plasmas, *Anal. Chem.*, 1994, **66**, 3371–3378.
44 J. W. Olesik and J. A. Kinzer, Measurement of monodisperse droplet desolvation in an inductively coupled plasma using droplet size dependent peaks in Mie scattering intensity, *Spectrochim. Acta, Part B*, 2006, **61**, 696–704.
45 J. A. Kinzer, Capillary electrophoresis-inductively coupled plasma spectrometry (CE-ICP): elemental speciation and fundamental studies of matrix effects in the ICP, PhD thesis, The Ohio State University, 1997.
46 A. C. Lazar and P. B. Farnsworth, Matrix effect studies in the inductively coupled plasma with monodisperse droplets.

Part II: the influence of matrix on spatially integrated ion density, *Appl. Spectrosc.*, 1999, **53**, 465–470.
47 A. C. Lazar and P. B. Farnsworth, Investigation of the analytical performance of an MDMI-ICP-AES system, *Appl. Spectrosc.*, 1997, **51**, 617–624.
48 J. W. Olesik, L. J. Smith and E. J. Williamsen, Signal fluctuations due to individual droplets in inductively coupled plasma atomic emission spectrometry, *Anal. Chem.*, 1989, **61**, 2002–2008.
49 C. A. Monnig and S. R. Koirtyohann, Mie scattering from sample aerosol inside the inductively coupled plasma, *Anal. Chem.*, 1985, **57**, 2533–2536.
50 R. K. Winge, J. S. Crain and R. S. Houk, A high speed photographic study of plasma fluctuations and undissociated particles in ICP-MS, *J. Anal. At. Spectrom.*, 1991, **6**, 601–604.
51 R. S. Houk, R. K. Winge and X. Chen, High speed photographic study of wet droplets and solid particles in the inductively coupled plasma, *J. Anal. At. Spectrom.*, 1997, **12**, 1139–1148.
52 D. B. Aeschliman, S. J. Bajic, D. P. Baldwin and R. S. Houk, High-speed digital photographic study of an inductively coupled plasma during laser ablation: comparison of dried solution aerosols from a microconcentric nebulizer and solid particles from laser ablation, *J. Anal. At. Spectrom.*, 2003, **18**, 1008–1014.
53 D. C. Perdian, S. J. Bajic, D. P. Baldwin and R. S. Houk, Time-resolved studies of particle effects in laser ablation inductively coupled plasma-mass spectrometry-part 1, *J. Anal. At. Spectrom.*, 2009, **23**, 325–335.
54 K. Jorabchi, R. G. Brennan, J. A. Levine and A. Montaser, Interferometric droplet imaging for *in situ* aerosol characterization in an inductively couple d plasma, *J. Anal. At. Spectrom.*, 2006, **21**, 839–846.
55 S. Groh, C. C. Garcia, A. Murtazin, V. Horvatic and K. Niemax, Local effects of atomizing analyte droplets on the plasma parameters of the inductively coupled plasma, *Spectrochim. Acta, Part B*, 2009, **64**, 247–254.
56 S. Groh, P. Diwakar, C. C. Garcia, A. Murtazin, D. W. Hahn and K. Niemax, 100% efficient sub-nanoliter sample introduction in laser induced breakdown spectroscopy and inductively coupled plasma spectrometry: implications for ultralow sample volumes, *Anal. Chem.*, 2010, **82**, 2568–2573.
57 A. Murtazin, S. Groh and K. Niemax, Investigation of sample introduction- and plasma-related matrix effects in inductively coupled plasma spectrometry applying single analyte droplet and particle injection, *Spectrochim. Acta, Part B*, 2012, **67**, 3–16.
58 K. Niemax, Considerations about the detection efficiency in inductively coupled plasma mass spectrometry, *Spectrochim. Acta, Part B*, 2012, **76**, 65–69.
59 S. Gschwind, L. Flamigni, J. Koch, O. Borovinskaya, S. Groh, K. Niemax and D. Günther, Capabilities of inductively coupled plasma mass spectrometry for the detection of nanoparticles carried by monodisperse micro-droplets, *J. Anal. At. Spectrom.*, 2011, **26**, 1166–1174.
60 L. Flamigni, J. Koch and D. Günther, Experimental and theoretical investigations about the vaporization of laser-produced aerosols and individual particles inside inductively coupled plasmas – implications for the extraction efficiency of ions prior to mass spectrometry, *Spectrochim. Acta, Part B*, 2012, **76**, 70–76.
61 J. Koch and D. Günther, Review of the state-of-the-art of laser ablation inductively coupled plasma mass spectrometry, *Appl. Spectrosc.*, 2011, **65**, 155A–162A.
62 O. Borovinskaya, M. Aghaei, L. Flamigni, B. Hattendorf, M. Tanner, A. Bogaerts and D. Günther, Diffusion- and velocity-driven spatial separation of analytes from single droplets entering an ICP off-axis, *J. Anal. At. Spectrom.*, 2014, **29**, 262–271.
63 R. M. Barnes and R. G. Schleicher, Computer simulation of RF induction-heated argon plasma discharges at atmospheric pressure for spectrochemical analysis-I. Preliminary investigations, *Spectrochim. Acta, Part B*, 1975, **30**, 109–134.
64 M. I. Boulos, Heating of powders in the fire ball of an induction plasma, *IEEE Trans. Plasma Sci.*, 1978, **6**, 91–106.
65 J. Mostaghimi and E. Pfender, Effects of metallic vapor on the properties of an argon arc plasma, *Plasma Chem. Plasma Process.*, 1984, **4**, 199–217.
66 P. Proulx, J. Mostaghimi and M. I. Boulos, Plasma–particle interaction effects in induction plasma modeling under dense loading conditions, *Int. J. Heat Mass Transfer*, 1985, **28**, 1327–1336.
67 P. Proulx, J. Mostaghimi and M. I. Boulos, Heating of powders in an r.f. inductively coupled plasma under dense loading conditions, *Plasma Chem. Plasma Process.*, 1987, **7**, 29–52.
68 J. Mostaghimi, P. Proulx and M. I. Boulos, An analysis of the computer modeling of the flow and temperature fields in an inductively coupled plasma, *Numerical Heat Transfer*, 1985, **8**, 187–201.
69 J. Mostaghimi, P. Proulx, M. I. Boulos and R. M. Barnes, Computer modeling of the emission patterns for a spectrochemical ICP, *Spectrochim. Acta, Part B*, 1985, **40**, 153–166.
70 J. Mostaghimi, P. Proulx and M. Boulos, A two temperature model of the inductively coupled rf plasma, *J. Appl. Phys.*, 1987, **61**, 1753–1760.
71 J. Mostaghimi and M. l Boulos, Effect of frequency on local thermodynamic equilibrium conditions in an inductively coupled argon plasma at atmospheric pressure, *J. Appl. Phys.*, 1990, **68**, 2643–2648.
72 M. EI-Hage, J. Mostaghimi and M. I. Boulos, A turbulent flow model for the rf inductively coupled plasma, *J. Appl. Phys.*, 1989, **65**, 4178.
73 J. Mostaghimi and M. I. Boulos, Two-dimensional electromagnetic field effects in induction plasma modelling, *Plasma Chem. Plasma Process.*, 1989, **9**, 25–44.
74 P. Yang, R. M. Barnes, J. Mostaghimi and M. I. Boulos, Application of a two-dimensional model in the simulation of an analytical inductively coupled plasma discharge, *Spectrochim. Acta, Part B*, 1989, **44**, 657–666.

75 Z. Njah, J. Mostaghimi and M. Boulos, Mathematical modelling of the 3-D mixing in an induction plasma reactor, *Int. J. Heat Mass Transfer*, 1993, **36**, 3909–3919.

76 G. Y. Zhao, J. Mostaghimi and M. I. Boulos, The induction plasma chemical reactor: part I. Equilibrium model, *Plasma Chem. Plasma Process.*, 1990, **10**, 133–150.

77 G. Y. Zhao, J. Mostaghimi and M. I. Boulos, The induction plasma chemical reactor: part II. Kinetic model, *Plasma Chem. Plasma Process.*, 1990, **10**, 151–166.

78 P. Proulx, J. Mostaghimi and M. I. Boulos, Radiative energy transfer in induction plasma modelling, *Int. J. Heat Mass Transfer*, 1991, **34**, 2571–2579.

79 M. Cai, A. Montaser and J. Mostaghimi, Two-temperature model for the simulation of atmospheric-pressure helium ICPs, *Appl. Spectrosc.*, 1995, **49**, 1390–1402.

80 M. Cai, A. Montaser and J. Mostaghimi, Computer simulation of atmospheric-pressure helium inductively coupled plasma discharges, *Spectrochim. Acta, Part B*, 1993, **48**, 789–807.

81 M. Cai, D. A. Haydar, A. Montaser and J. Mostaghimi, Computer simulation of argon–nitrogen and argon–oxygen inductively coupled plasmas, *Spectrochim. Acta, Part B*, 1997, **52**, 369–386.

82 S. Xue, P. Proulx and M. I. Boulos, Extended-field electromagnetic model for inductively coupled plasma, *J. Phys. D: Appl. Phys.*, 2001, **34**, 1897–1906.

83 P. Yang, J. A. Horner, N. N. Sesi and G. M. Hieftje, Comparison of simulated and experimental fundamental ICP parameters, *Spectrochim. Acta, Part B*, 2000, **55**, 1833–1845.

84 C. M. Benson, S. F. Gimelshein, D. A. Levin and A. Montaser, Simulation of droplet heating and desolvation in an inductively coupled plasma-part I, *Spectrochim. Acta, Part B*, 2001, **56**, 1097–1112.

85 C. M. Benson, S. F. Gimelshein, D. A. Levin and A. Montaser, *Modeling of droplet evaporation from a nebulizer in an inductively coupled plasma, presented at the 22nd Int. Symp. on Rarefied Gas Dynamics*, American Institute of Physics, 2001, pp. 246–253.

86 C. M. Benson, J. Zhong, S. F. Gimelshein, D. A. Levin and A. Montaser, Simulation of droplet heating and desolvation in inductively coupled plasma-part II: coalescence in the plasma, *Spectrochim. Acta, Part B*, 2003, **58**, 1453–1471.

87 J. A. Horner and G. M. Hieftje, Computerized simulation of mixed-solute-particle vaporization in an inductively coupled plasma, *Spectrochim. Acta, Part B*, 1998, **53**, 1235–1259.

88 Y. Shan and J. Mostaghimi, Numerical simulation of aerosol droplets desolvation in a radio frequency inductively coupled plasma, *Spectrochim. Acta, Part B*, 2003, **58**, 1959–1977.

89 V. Colombo, C. Panciatichi, A. Zazo, G. Cocito and L. Cognolato, Modeling, project, numerical simulation, and AES temperature diagnostics of an inductively coupled plasma torch for the deposition of high-purity fused silica for optical waveguide production, *IEEE Trans. Plasma Sci.*, 1997, **25**, 1073–1080.

90 D. Bernardi, V. Colombo, G. G. M. Coppa and A. D'Angola, Simulation of the ignition transient in rf inductively coupled plasma torches, *Eur. Phys. J. D*, 2001, **14**, 337–348.

91 D. Bernardi, V. Colombo, G. G. M. Coppa, E. Ghedini and A. Mentrelli, *Investigation on bistability in inductively coupled plasma torches with non-conventional coil, in Proc. 7th Eur. Conf. on Thermal Plasma Processes*, Strasbourg, France, 2002.

92 D. Bernardi, V. Colomboa, E. Ghedini and A. Mentrelli, Three-dimensional modeling of inductively coupled plasma torches, *Eur. Phys. J. D*, 2003, **22**, 119–125.

93 D. Bernardi, V. Colombo, E. Ghedini and A. Mentrelli, Three-dimensional modeling of inductively coupled plasma torches, *Pure Appl. Chem.*, 2005, **77**, 359–372.

94 D. Bernardi, V. Colomboa, E. Ghedini and A. Mentrelli, Three-dimensional effects in the modeling of ICPTs-part I: fluid dynamics and electromagnetic, *Eur. Phys. J. D*, 2003, **25**, 271–277.

95 D. Bernardi, V. Colomboa, E. Ghedini and A. Mentrelli, Three-dimensional effects in the modeling of ICPTs-part II: induction coil and torch geometry, *Eur. Phys. J. D*, 2003, **25**, 279–285.

96 V. Colombo, E. Ghedini and J. Mostaghimi, Three-dimensional modeling of an inductively coupled plasma torch for spectroscopic analysis, *IEEE Trans. Plasma Sci.*, 2008, **36**, 1040–1041.

97 D. Bernardi, V. Colombo, E. Ghedini, A. Mentrelli and T. Trombetti, 3-D numerical simulation of fully-coupled particle heating in ICPTs, *Eur. Phys. J. D*, 2004, **28**, 423–433.

98 D. Bernardi, V. Colombo, E. Ghedini, A. Mentrelli and T. Trombetti, 3-D numerical analysis of powder injection in inductively coupled plasma torches, *IEEE Trans. Plasma Sci.*, 2005, **33**, 424–425.

99 V. Colombo, E. Ghedini and P. Sanibondi, Three-dimensional investigation of particle treatment in an rf thermal plasma with reaction chamber, *Plasma Sources Sci. Technol.*, 2010, **19**, 065024–065036.

100 D. Bernardi, V. Colombo, E. Ghedini and A. Mentrelli, 3-D turbulent modeling of an ICPT with detailed gas injection section, *IEEE Trans. Plasma Sci.*, 2005, **33**, 426–427.

101 V. Colombo, A. Concetti, E. Ghedini, M. Gherardi and P. Sanibondi, Three-dimensional time-dependent large eddy simulation of turbulent flows in an inductively coupled thermal plasma torch with a reaction chamber, *IEEE Trans. Plasma Sci.*, 2011, **39**, 2894–2895.

102 V. Colombo, E. Ghedini and P. Sanibondi, Two-temperature thermodynamic and transport properties of argon–hydrogen and nitrogen–hydrogen plasmas, *J. Phys. D: Appl. Phys.*, 2009, **42**, 055213–055224.

103 V. Colombo, E. Ghedini and P. Sanibondi, Two-temperature thermodynamic and transport properties of carbon–oxygen plasmas, *Plasma Sources Sci. Technol.*, 2011, **20**, 035003–035010.

104 V. Colombo, E. Ghedini, M. Gherardi and P. Sanibondi, Modelling for the optimization of the reaction chamber in silicon nanoparticle synthesis by a radio-frequency induction thermal plasma, *Plasma Sources Sci. Technol.*, 2012, **21**, 055007–055016.

105 V. Colombo, E. Ghedini, M. Gherardi, P. Sanibondi and M. Shigeta, A two-dimensional nodal model with

turbulent effects for the synthesis of Si nano-particles by inductively coupled thermal plasmas, *Plasma Sources Sci. Technol.*, 2012, **21**, 025001–025012.
106 M. Shigeta, T. Sato and H. Nishiyama, Computational simulation of a particle-laden rf inductively coupled plasma with seeded potassium, *Int. J. Heat Mass Transfer*, 2004, **47**, 707–716.
107 M. Shigeta, T. Sato and H. Nishiyama, Numerical simulation of a potassium-seeded turbulent rf inductively coupled plasma with particles, *Thin Solid Films*, 2003, **435**, 5–12.
108 H. Nishiyama and M. Shigeta, Numerical simulation of an rf inductively coupled plasma for functional enhancement by seeding vaporized alkali metal, *Eur. Phys. J.: Appl. Phys.*, 2002, **18**, 125–133.
109 M. Shigeta and H. Nishiyama, Numerical analysis of metallic nanoparticle synthesis using rf inductively coupled plasma flows, *J. Heat Transfer*, 2005, **127**, 1222–1230.
110 M. Shigeta and T. Watanabe, Numerical analysis for co-condensation processes in silicide nanoparticle synthesis using induction thermal plasmas at atmospheric pressure conditions, *J. Mater. Res.*, 2005, **20**, 2801–2811.
111 M. Shigeta, Three-dimensional flow dynamics of an argon rf plasma with dc jet assistance: a numerical study, *J. Phys. D: Appl. Phys.*, 2013, **46**, 015401–015413.
112 M. Shigeta, Time-dependent 3D simulation of an argon rf inductively coupled thermal plasma, *Plasma Sources Sci. Technol.*, 2012, **21**, 055029–055043.
113 M. Shigeta, T. Watanabe and H. Nishiyama, Numerical investigation for nano-particle synthesis in an rf inductively coupled plasma, *Thin Solid Films*, 2004, **457**, 192–200.
114 M. Shigeta and T. Watanabe, Numerical investigation of cooling effect on platinum nanoparticle formation in inductively coupled thermal plasmas, *J. Appl. Phys.*, 2008, **103**, 074903–074918.
115 T. Watanabe, M. Shigeta and N. Atsuchi, Two-temperature chemically-non-equilibrium modeling of argon induction plasmas with diatomic gas, *Int. J. Heat Mass Transfer*, 2006, **49**, 4867–4876.
116 N. Atsuchi, M. Shigeta and T. Watanabe, Modeling of non-equilibrium argon–oxygen induction plasmas under atmospheric pressure, *Int. J. Heat Mass Transfer*, 2006, **49**, 1073–1082.
117 D. Benoy, Modeling of thermal argon plasmas, PhD thesis, Eindhoven University of Technology, 1993.
118 B. Bottin, D. Vanden Abeele, M. Carbonaro, G. Degrez and G. S. R Sarma, Thermodynamic and transport properties for inductive plasma modeling, *J. Thermophys. Heat Transfer*, 1999, **13**, 343–350.
119 D. Vanden Abeele and G. Degrez, Efficient computational model for inductive plasma flows, *AIAA J.*, 2002, **38**, 234–242.
120 G. Degrez, D. Vanden Abeele, P. Barbante and B. Bottin, Numerical simulation of inductively coupled plasma flows under chemical non-equilibrium, *Int. J. Numer. Methods Heat Fluid Flow*, 2004, **14**, 538–558.
121 T. E. Magin, M. Panesi, P. Rini, D. Vanden Abeele and G. Degrez, *Simulation of supersonic flows in inductively coupled plasma tunnels, in Proc. 3rd Int. Conf. on Computational Fluid Dynamics, ICCFD3*, Toronto, 2004, pp. 489–494.
122 D. J. Douglas and J. B. French, Gas dynamics of the inductively coupled plasma mass spectrometry interface, *J. Anal. At. Spectrom.*, 1988, **3**, 743–747.
123 R. L. Spencer, J. Krogel, J. Palmer, A. Payne, A. Sampson, W. Somers and C. N. Woods, Modeling the gas flow upstream and in the sampling nozzle of the inductively coupled plasma mass spectrometer *via* the direct simulation Monte Carlo algorithm, *Spectrochim. Acta, Part B*, 2009, **64**, 215–221.
124 R. L. Spencer, N. Taylor and P. B. Farnsworth, Comparison of calculated and experimental flow velocities from the sampling cone of an inductively coupled plasma mass spectrometer, *Spectrochim. Acta, Part B*, 2009, **64**, 921–924.
125 H. Lindner and A. Bogaerts, Multi-element model for the simulation of inductively coupled plasmas: effects of helium addition to the central gas stream, *Spectrochim. Acta, Part B*, 2011, **66**, 421–431.
126 H. Lindner, A. Murtazin, S. Groh, K. Niemax and A. Bogaerts, Simulation and experimental studies on plasma temperature, flow velocity and injector diameter effects for an inductively coupled plasma, *Anal. Chem.*, 2011, **83**, 9260–9266.
127 M. Aghaei, H. Lindner and A. Bogaerts, Effect of a mass spectrometer interface on inductively coupled plasma characteristics: a computational study, *J. Anal. At. Spectrom.*, 2012, **27**, 604–610.
128 M. Aghaei, H. Lindner and A. Bogaerts, Optimization of operating parameters for inductively coupled plasma mass spectrometry: a computational study, *Spectrochim. Acta, Part B*, 2012, **76**, 56–64.
129 M. Aghaei, H. Lindner and A. Bogaerts, Effect of sampling cone position and diameter on the gas flow dynamics in an ICP, *J. Anal. At. Spectrom.*, 2013, **28**, 1485–1492.
130 M. Aghaei, L. Flamigni, H. Lindner, D. Gunther and A. Bogaerts, Occurrence of gas flow rotational motion inside the ICP torch: a computational and experimental study, *J. Anal. At. Spectrom.*, 2014, **29**, 249–261.
131 M. Aghaei, Computational study of the inductively coupled plasma mass spectrometry (ICP-MS), PhD thesis, University of Antwerp, 2014.
132 M. Aghaei and A. Bogaerts, Particle transport through an inductively coupled plasma torch: elemental droplet evaporation, *J. Anal. At. Spectrom.*, 2016, **31**, 631–641.
133 M. Aghaei, H. Lindner and A. Bogaerts, Ion clouds in the ICP torch: a closer look through computations, *Anal. Chem.*, 2016, **88**, 8005–8018.
134 *ANSYS FLUENT 16 Documentation*, Theory Guide, 2015.
135 D. R. Lide, *CRC Handbook of Chemistry and Physics*, CRC Press LLC, Boca Raton, Florida, 83rd edn, 2002.

136 H. Ounis, G. Ahmadi and J. B. McLaughlin, Brownian diffusion of submicrometer particles in the viscous sublayer, *J. Colloid Interface Sci.*, 1991, **143**, 266–277.
137 W. E. Ranz and W. R. Marshall, Vaporation from drops, part I, *Chem. Eng. Prog.*, 1952, **48**, 141–146.
138 W. E. Ranz and W. R. Marshall, Evaporation from drops, part II, *Chem. Eng. Prog.*, 1952, **48**, 173–180.
139 A. B. Murphy, A comparison of treatments of diffusionin thermal plasmas, *J. Phys. D: Appl. Phys.*, 1996, **29**, 1922–1932.
140 H. Lindner, Untersuchungen zur Partikelverteilung und zusammensetzung beim Laserabtrag, PhD thesis, Universität Dortmund, 2004.
141 C. B. Boss and G. M. Hieftje, Calculation of the velocity of a desolvating aerosol droplet in an analytical flame, *Anal. Chem.*, 1977, **49**, 2112–2114.
142 P. Farnsworth, R. Spencer, W. N. Radicic, N. Taylor, J. Macedone and H. Ma, A comparison of ion and atom behavior in the first stage of an inductively coupled plasma mass spectrometer vacuum interface: evidence of the effect of an ambipolar electric field, *Spectrochim. Acta, Part B*, 2009, **64**, 905–910.
143 J. E. Patterson, B. S. Duersch and P. B. Farnsworth, Optically determined velocity distributions of metastable argon in the second stage of an inductively coupled plasma mass spectrometer, *Spectrochim. Acta, Part B*, 1999, **54**, 537–544.
144 W. N. Radicic, J. B. Olsen, R. V. Nielson, J. H. Macedone and P. B. Farnsworth, Characterization of the supersonic expansion in the vacuum interface of an inductively coupled plasma mass spectrometer by high-resolution diode laser spectroscopy, *Spectrochim. Acta, Part B*, 2006, **61**, 686–695.
145 A. A. Mills, J. H. Macedone and P. B. Farnsworth, High resolution imaging of barium ions and atoms near the sampling cone of an inductively coupled plasma mass spectrometer, *Spectrochim. Acta, Part B*, 2006, **61**, 1039–1049.
146 M. W. Blades and G. Horlick, The vertical spatial characteristics of analyte emission in the inductively coupled plasma, *Spectrochim. Acta, Part B*, 1981, **36**, 861–880.
147 G. C. Y. Chan and G. M. Hieftje, Fundamental characteristics of plasma-related matrix-effect cross-over points in inductively coupled plasma-atomic emission spectrometry, *J. Anal. At. Spectrom.*, 2009, **24**, 439–450.
148 J. A. Horner, S. A. Lehn and G. M. Hieftje, Computerized simulation of aerosol-droplet desolvation in an inductively coupled plasma, *Spectrochim. Acta, Part B*, 2002, **57**, 1025–1042.
149 G. M. Hieftje and H. V. Malmstadt, Unique system for studying flame spectrometric processes, *Anal. Chem.*, 1968, **40**, 1860–1867.
150 N. C. Clampitt and G. M. Hieftje, Mechanism of desolvation of sample droplets in flame spectrometry, *Anal. Chem.*, 1972, **44**, 1211–1218.